Global Biogeochemical Cycles

RESEARCH ARTICLE
10.1029/2020GB006574

Special Section:
Understanding Carbon-Climate Feedbacks

Amplification of the Ocean Carbon Sink During El Niños: Role of Poleward Ekman Transport and Influence on Atmospheric CO_2

Enhui Liao[1], Laure Resplandy[1], Junjie Liu[2], and Kevin W. Bowman[2]

[1]Department of Geosciences, Princeton University, Princeton, NJ, USA, [2]Jet Propulsion Laboratory, California Institute of Technology, Pasadena, CA, USA

Abstract Amplification of the ocean carbon sink during El Niño events partially offset terrestrial biosphere carbon losses to the atmosphere, but uncertainties in the magnitude, timing, and spatial extent of the ocean response confound our understanding of the global carbon budget and its sensitivity to climate. Here, we examine the mechanisms controlling the anomalous tropical Pacific Ocean CO_2 drawdown during El Niño events harnessing multidecadal ocean pCO_2 observations in conjunction with a state-of-the-art ocean biogeochemical model. We show that poleward Ekman transport dramatically amplifies the near-equatorial pCO_2 anomaly identified in prior work and that this amplification varies considerably between El Niño events. During central Pacific events, the CO_2 flux anomaly can vary up to fourfold between events (2002/2003 vs. 2015/2016), but it always recedes during the boreal winter to spring transition and the poleward transport of the anomaly mostly extends into the Northern Hemisphere. During eastern Pacific events characterized by an equatorially centered intertropical convergence zone (e.g., 1997/1998), the intense CO_2 flux anomaly persists into boreal summer and can extend further into the Southern Hemisphere. The hemispheric asymmetry (northward vs. southward extension) and the termination (boreal winter/spring for central Pacific events vs. boreal summer for eastern Pacific events) of the ocean CO_2 response are tied to the El Niño dynamics in the near-equatorial region and also how it is amplified by poleward Ekman transport. Finally, we evaluate how differences in the ocean response influence atmospheric CO_2 and discuss the potential of atmospheric CO_2 satellite data to provide observational constraints.

Key Points:
- Anomalous ocean CO_2 drawdown originated from near-equatorial Pacific Ocean during El Niño is amplified by poleward Ekman transport
- Equatorially centered ITCZ during extreme eastern Pacific El Niño events yields a more intense and long-lasting ocean CO_2 drawdown
- Atmospheric CO_2 satellite data could constrain spatiotemporal differences in CO_2 drawdown between events

Supporting Information:
- Supporting Information S1

Correspondence to:
L. Resplandy,
laurer@princeton.edu

Citation:
Liao, E., Resplandy, L., Liu, J., & Bowman, K. W. (2020). Amplification of the ocean carbon sink during El Niños: Role of poleward Ekman transport and influence on atmospheric CO_2. *Global Biogeochemical Cycles*, *34*, e2020GB006574. https://doi.org/10.1029/2020GB006574

Received 14 FEB 2020
Accepted 15 JUN 2020
Accepted article online 24 JUN 2020

1. Introduction

The El Niño–Southern Oscillation (ENSO) is the primary source of interannual variability in atmospheric CO_2 concentrations (e.g., Bacastow, 1976; Jones et al., 2001; Keeling et al., 1995; Keeling & Revelle, 1985). Observed atmospheric CO_2 growth rates during El Niño events are 0.5 to 1.2 ppm/yr larger than normal years (Betts et al., 2016). These larger growth rates largely stem from the net reduced carbon uptake by the tropical land biosphere (e.g., Bowman et al., 2017; Cox et al., 2013; Liu et al., 2017; Rödenbeck et al., 2018; Sellers et al., 2018). The reduced CO_2 uptake on land is, however, partly compensated by an anomalous ocean CO_2 drawdown in the tropical Pacific Ocean (e.g., Bacastow, 1976; Feely et al., 1999, 2002; Ishii et al., 2014; Keeling & Revelle, 1985). Recent satellite observations of column atmospheric CO_2 suggest that the role of the ocean in offsetting the land response strongly varied over the course of the 2015/2016 El Niño event (Chatterjee et al., 2017). The spatiotemporal evolution of the ocean response to El Niño is however still poorly constrained (McKinley et al., 2017) but critical to an accurate partitioning of ocean and land carbon fluxes. Better understanding of these processes could lead to a more adroit use of interannual variability to estimate the climate sensitivity of land and ocean carbon cycles (e.g., Cox et al., 2013; Kwiatkowski et al., 2017) and a reduction in uncertainty of the year-to-year imbalance in the global carbon budget (Le Quéré et al., 2018).

The occurrence of an anomalous ocean CO_2 drawdown in response to El Niño events has long been recognized (Bacastow, 1976; Keeling & Revelle, 1985). Prior studies based on observations, ocean model, and atmospheric inversions suggest that the ocean drawdown varies between 0.1 and 0.7 PgC/yr depending on the El Niño event, the period during the event and the region that is considered (Feely et al., 1999; Ishii et al., 2014; Le Quéré et al., 2000; McKinley, Rödenbeck, et al., 2004; Peylin et al., 2013; Rödenbeck

et al., 2014, 2015). Such a broad range in the ocean drawdown is to be expected. The magnitude, timing, and spatial patterns of the physical (e.g., warming, precipitation, and winds) and biological (e.g., phytoplankton production) response associated with El Niño events strongly vary temporally and spatially between events (e.g., Behrenfeld et al., 2001; McPhaden et al., 2006; Racault et al., 2017; Wang et al., 2017, 2019; Wang & Picaut, 2004). In particular, extreme events in 1982/1983 and 1997/1998, referred to as eastern Pacific El Niño events, were associated with westerly wind anomalies across the basin and an equatorially centered intertropical convergence zone, which yielded a long-lasting collapse of the easterly trade winds and equatorial upwelling in the eastern Pacific (Kao & Yu, 2009; Kug et al., 2009; Lengaigne & Vecchi, 2010; Vecchi & Harrison, 2006). In contrast, during events referred to as central Pacific El Niño events (e.g., 2003/2003) westerly wind anomalies were confined to the western and central Pacific leading to a weaker response in the eastern Pacific and a prompter return to normal conditions (Ashok et al., 2007). These dynamical differences influence the ecosystem response, with larger reduction in biological production and chlorophyll observed in regions of higher surface temperature anomaly (Gierach et al., 2012; Turk et al., 2011). Yet, little is known about how these physical and biological differences influence the air-sea CO_2 flux response. Here, we leverage 30+ years of available ocean pCO_2 observations and the results of an ocean biogeochemical model to examine the evolution of the ocean CO_2 response to El Niño and contrast the differences between events, with an emphasis on the mechanisms controlling the magnitude, timing, and spatial pattern of the anomalous CO_2 drawdown.

During non-El Niño conditions, the tropical Pacific Ocean is the largest natural oceanic source of CO_2 to the atmosphere. The CO_2 outgassing is strongest in the eastern part of the basin where observed differences in partial pressure of CO_2 between the ocean and the atmosphere reach 100–150 uatm (Sutton, Feely, et al., 2014). In the eastern tropical Pacific and along the equator in the central Pacific, wind-driven upwelling associated with easterly winds supplies subsurface dissolved inorganic carbon (DIC) and nutrients to the ocean surface. This supply of DIC surpasses the biological drawdown sustained by the upwelling of nutrients (photosynthesis) and maintains high ocean surface pCO_2 and an intense CO_2 outgassing (outgassing >10 $gC/m^2/yr$, (Feely et al., 2002; Landschützer et al., 2014; Rödenbeck et al., 2013; Takahashi et al., 1997; Wanninkhof et al., 1996). In the western part of the basin, however, the deep thermocline and freshwater cap associated with the warm pool limit the supply of DIC and nutrients to the surface, resulting in low dynamical and biological influences (Feely et al., 2002; Inoue et al., 2001). The oceanic and atmospheric pCO_2 in this region are close to equilibrium and the air-sea CO_2 flux is small (outgassing <3 $gC/m^2/yr$ in Landschützer et al., 2014; Rödenbeck et al., 2013).

During El Niño events, the oceanic source of CO_2 in the eastern and central Pacific drops (Figures 1 and 2). The first-order physical and biological processes governing this anomalous CO_2 drawdown have been identified (e.g., Behrenfeld et al., 2001; Chavez et al., 1999; Doney et al., 2009; Feely et al., 2002; Le Quéré et al., 2000): Easterly winds weaken, eastward propagating Kelvin wave deepens the thermocline in the eastern equatorial Pacific, and the freshwater cap associated with the warm pool extends to the central equatorial Pacific (McPhaden et al., 1998; Wang et al., 2012). Combined, these processes yield a weaker upwelling of DIC and a reduction in ocean surface pCO_2 and CO_2 outgassing along the equator (e.g., Doney et al., 2009; Eddebbar et al., 2017; Feely et al., 2002; Le Quéré et al., 2000). Concomitant changes that could reinforce the CO_2 drawdown are the diminution of CO_2 solubility due to warm sea surface temperature (SST) anomalies (Jones et al., 2001) and the reduced wind speeds in the central equatorial Pacific (Boutin et al., 1999; McKinley, Follows, et al., 2004). In contrast, the reduced upwelling of nutrients limits the biological production and uptake of DIC and dampen the CO_2 drawdown (Behrenfeld et al., 2001; Chavez et al., 1999; Le Borgne et al., 2002; Racault et al., 2017). Observations from the Tropical Atmosphere Ocean/Triangle Trans-Ocean Buoy Network (TAO/TRITON) array along the equator show that the central Pacific Ocean can reach equilibrium with the atmosphere and even temporarily become a slight sink of CO_2 during some El Niño events (e.g., mooring at 155°W in 1997/1998 and mooring at 170°W in 2009/2010, Sutton, Feely, et al., 2014).

In this paper, we examine how the physical and biological changes associated with El Niño events control the air-sea CO_2 flux. We show that the temporal evolution and magnitude of the ocean CO_2 drawdown are connected to the ocean pCO_2 anomaly in the near-equatorial region and how this anomaly is amplified by poleward Ekman transport to the southern and northern tropical Pacific Ocean. The paper is structured

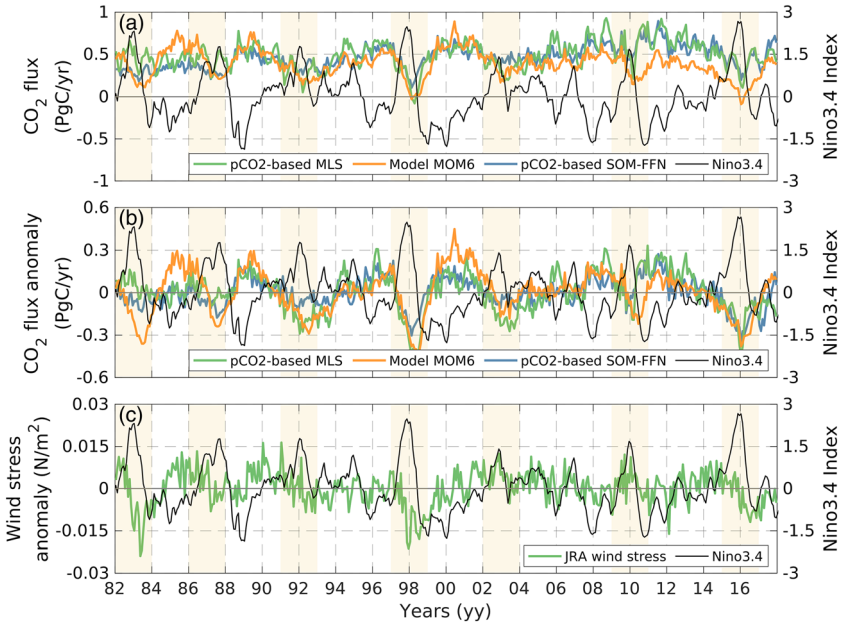

Figure 1. Time-series of (a) the air-sea CO_2 flux (negative to the ocean) and (b) the air-sea CO_2 flux interannual anomaly (negative is anomalous uptake by ocean) integrated over the tropical Pacific Ocean (15°N to 15°S and 160°E to the South American coastline) in two pCO_2-based data products and in the ocean model MOM6, and (c) the wind stress interannual anomaly in the eastern equatorial Pacific Ocean (2°N to 2°S, 210–270°E). Observational pCO_2-based products are from Rödenbeck et al. (2013) mixed-layer scheme (MLS) and Landschützer et al. (2014) neural network interpolation (SOM-FFN). Wind stress are from the atmospheric reanalysis JRA55-do v1.3. Niño 3.4 index is computed from HadISST1 data.

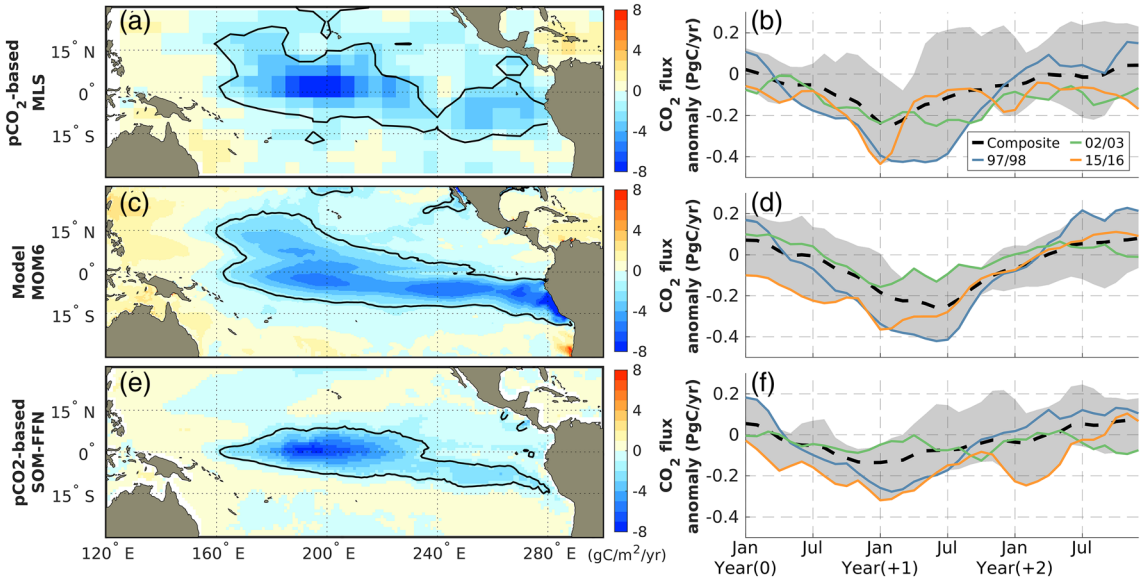

Figure 2. El Niño air-sea CO_2 flux anomaly from two observational pCO_2-based products (a-b, e-f) and simulated in the MOM6 model (c-d). Two-year mean composite maps (January of Year(0) to December of Year(+1)) and time series are integrated over the tropical Pacific Ocean (15°N to 15°S and 160°E to the south American coastline). The composite includes six El Niño events. Negative values are anomalous uptake by the ocean. Contours delimit the regions of intense anomalous drawdown (-1.6 gC/m^2/yr) used for the mixed-layer budget. Observational pCO_2-based products are from Rödenbeck et al. (2013) mixed-layer scheme (MLS, a-b) and Landschützer et al. (2014) neural network interpolation (SOM-FFN, e-f).

as follows: Section 2 describes the observations, the model data, and the methods used. In section 3, we first examine the mechanisms controlling the mean CO_2 flux response to El Niño events and identify the poleward amplification by Ekman transport (composite response to the six most recent El Niño events) and then show that this poleward amplification strongly varies between extreme eastern Pacific and central Pacific El Niño events. Finally, we explore how differences in the oceanic response between events can influence atmospheric CO_2. In section 4, we summarize the results and discuss limitations and implications of our study.

2. Model, Methods and Data

2.1. Observational Data

2.1.1. Ocean Surface pCO_2 and Air-Sea CO_2 Fluxes

We use two global monthly gridded products of the ocean surface pCO_2 and air-sea CO_2 flux, both derived from Surface Ocean CO_2 Atlas (SOCAT) pCO_2 database (Bakker et al., 2016). The mixed-layer scheme of Rödenbeck et al. (2013) referred to as the pCO_2-based MLS product, and the neural network interpolation of Landschützer et al. (2014) referred to as the pCO_2-based SOM-FFN product.

2.1.2. Mooring Data

The tropical atmosphere ocean (TAO) array data are downloaded from Pacific Marine Environmental Laboratory NOAA (McPhaden et al., 1998; Sutton, Sabine, et al., 2014). At longitude 190°E, CO_2 TAO array data are recorded by three moorings: 2°S (year 1998–2004), 0°N (year 2005–2015), and 2°N (year 2007–2008). Since a 2-by-2 degree box is used in the model evaluation, the three moorings are combined together as one data set at 190°E. We also use data from the TAO moorings at 220°E, 0°N and 250°E, 0°N. For more data temporal coverage, two sets of ΔpCO_2 are computed using surface ocean and atmospheric CO_2 mole fraction (xCO_2 dry) and pCO_2 (sat, 100% humidity). The differences between them are small compared with interannual variability.

2.1.3. Other Data

For model evaluation, chlorophyll, nitrate (NO_3), phosphate (PO_4), DIC, SST, sea surface salinity (SSS), and mixing layer depth (MLD) are selected to compare with observational data. Chlorophyll is from GlobColour (Maritorena et al., 2010). NO_3 and PO_4 are from World Ocean Atlas version 2013 and DIC is from GLODAP v2 (Olsen et al., 2016). SST is Optimum Interpolation SST (OISST) v2 (Banzon et al., 2016) and SSS is from Aquarius CAP (Yueh et al., 2014) and SMAP CAP (Meissner et al., 2018) salinity data. MLD (density criteria of 0.03 kg/m^3) is from de Boyer Montégut et al. (2004) and thermocline depth (20°C depth) is computed from Argo gridded temperature data (Roemmich & Gilson, 2009). The observed Niño 3.4 index is downloaded from the Earth System Research Laboratory NOAA (Rayner et al., 2003). It is calculated from HadISST1 data as the area-averaged SST anomaly between 5°S to 5°N and 170–120°W compared to the 1981–2010 baseline.

2.2. Ocean Model Description

We used the Geophysical Fluid Dynamics Laboratory (GFDL) global ocean/sea ice model, which includes the Modular Ocean Model version 6 (MOM6) and the Sea Ice Simulator version 2 (SIS2). This model version, labeled as the fourth generation of ocean-ice models (OM4), serves as the ocean/sea ice component for the GFDL climate and Earth system models (CM4 and ESM 4) contributing to the Coupled Model Intercomparison Project (CMIP6) and Ocean Model Intercomparison Project (OMIP6) versions 6 (see details of the configuration in Adcroft et al., 2019). The version of OM4 adopted here is OM4P5 with a horizontal resolution of 0.5° and eddy parameterization. On the vertical, it includes 75 hybrid isopycnal-z* coordinate, including a z* coordinate near the surface (about 2 m thick layers in the upper 20 m in the tropical Pacific Ocean) and a modified potential density coordinate below (see Adcroft et al., 2019 for details on the grid). Sea surface temperature (SST) and salinity (SSS) relaxations are turned off in the simulation. This ocean/sea ice model is coupled with the biogeochemical module Carbon Ocean Biogeochemistry and Lower Trophics version 2 (COBALT v2), which includes 33 state variables, including nutrients (nitrate, phosphate, and iron), silicate, three phytoplankton groups, three zooplankton groups, three dissolved organic carbon pools, one particulate detritus pool, oxygen, and the carbonate system (Stock et al., 2014b). Details about the planktonic food web dynamics in COBALT, and global assessments of large-scale carbon fluxes through the food web (e.g., net primary and zooplankton production) can be found in Stock et al. (2014b).

The ocean model is forced by the 55 km horizontal resolution Japanese 55 year atmospheric reanalysis data set (JRA55-do) version 1.3 at a 3-hr frequency (Tsujino et al., 2018) and atmospheric pCO_2 data from the Earth System Research Laboratory (Joos & Spahni, 2008). We use atmospheric pCO_2 global average for the 1959–1978 period and latitudinally resolved for the 1979–2018 period. The model was spun up from rest for 81 years by repeating year 1959 of the JRA55-do v1.3 forcing. Temperature, salinity, nutrients (nitrate, phosphate, and silicate), and oxygen were initialized from World Ocean Atlas version 2013 (Garcia, Boyer, et al., 2013; Garcia, Locarnini, et al., 2013; Locarnini et al., 2013; Zweng et al., 2013). Initial dissolved inorganic carbon (DIC) and alkalinity (Alk) are from GLODAP v2 (Olsen et al., 2016). The initial DIC is corrected for the accumulation of anthropogenic carbon to match the level expected in 1959 using the data-based estimate of ocean anthropogenic carbon content (Khatiwala et al., 2013). Other COBALT tracer initial conditions (e.g., ammonium, calcium carbonate) are from a preindustrial GFDL-ESM 2 M-COBALT simulation (Stock et al., 2014a). At the end of the 81-year spin-up, the model has reached a near-equilibrium between atmospheric pCO_2 and surface ocean pCO_2, with a drift in global air-sea CO_2 flux <0.004 PgC/yr over the last 10 years of spin-up. The hindcast simulation is then performed from 1959 to 2018.

The air sea CO_2 flux (FCO_2) is computed using the following bulk formula:

$$FCO_2 = k_w \alpha (pCO_{2w} - pCO_{2a}) \quad (1)$$

where pCO_{2a} is the atmospheric partial pressure of CO_2, pCO_{2w} is the sea surface partial pressure of CO_2, α denotes the solubility of CO_2, computed using the temperature- and salinity-dependent formulation of Weiss and Price (1980), and k_w is the CO_2 gas transfer coefficient based on a quadratic wind speed formulation (Wanninkhof, 1992) using wind speeds from JRA55-do v1.3. Wind can be a source of bias in air sea flux calculation (e.g., Chiodi et al., 2019; Cronin et al., 2019; Sutton et al., 2017). Comparison of the wind speed from the JRA55-do v1.3 and the TAO equatorial mooring observations shows, however, a good agreement, in line with Taboada et al. (2019) which showed a clear improvement in quality between older wind product (e.g., NCEP) and the JRA55-do v1.3 reanalysis (see discussion of model biases in sections 2.3 and 3.1). The two coefficients computation follows Najjar and Orr (1998). The sign convention is that positive FCO_2 denotes an oceanic outgassing of CO_2.

2.3. Climatological Mean State and Interannual Variability in the Tropical Pacific Ocean

We define the tropical Pacific Ocean as the region between 15°S to 15°N and from 160°E to the South American coastline. Model and observation climatological fields are computed for the period January 1982 to December 2017 except when observations covered a shorter period, that is, satellite chlorophyll climatology is computed for 1997–2018, satellite SSS climatology is computed for 2012–2018, and Argo float fields climatologies are computed for 2004–2018. The ocean model reproduces the observed climatological physical and biogeochemical features in the tropical Pacific Ocean including the east–west gradient between the warm pool in the western Pacific, which is characterized by low DIC, SSS, nitrate, chlorophyll and surface ocean pCO_2, and the cold equatorial and coastal upwelling systems in the central and eastern Pacific, which are characterized by high DIC, SSS, nitrate, chlorophyll, and surface ocean pCO_2 (Figures S1–S3 in the supporting information). Simulated surface salinity is biased high in the northern (+0.4 salinity unit) and southern (+0.2 salinity unit) subtropical gyres and the central equatorial Pacific (+0.3 salinity unit). This bias originates in the subtropical gyres where too shallow mixed-layer depths reinforce the effect of evaporation on surface salinity and transported by subtropical mode water formed in the gyres into the Equatorial Undercurrent (Figure S1). This subsurface bias is then brought to the surface by vertical dynamics (mixing and advection) in the central equatorial Pacific. This bias impact the mean vertical structure in the equatorial region and probably explains the shallow equatorial mixed-layer and the associated interannual biases in SSS and ocean surface pCO_2 (see details in section 3.1).

Deseasonalized interannual anomalies in model and observed variables (except the Niño3.4 index which is downloaded from the NOAA website, see section 2.1 above) are computed by first removing the long-term 1982–2017 linear trend, then subtracting the 1982–2017 climatological monthly value, and finally using a 3-month moving average filter. Because the mooring pCO_2 data are not continuous, we use trend and climatological monthly values from the pCO_2-based MLS product to compute interannual anomalies from mooring pCO_2 and xCO_2 data. The model interannual variability is described and evaluated in section 3.

We compute an El Niño monthly composite that averages six El Niño events (1986/1987, 1991/1992, 1997/1998, 2002/2003, 2009/2010, and 2015/2016). We did not use the 1982–1983 event in the composite due to the poor observational coverage and the inconsistencies between the two observational pCO_2-based products during this event (see Figure 1). We use the notation Year(0) to refer to the first year of the El Niño event (e.g., 1986, 1991, 1997, ... 2015), and Year(+1) and Year(+2) for the following years (e.g., Year(+1) = 1987, 1992, 1998, ... 2016).

2.4. Identification of the Mechanisms Controlling the Ocean CO_2 Drawdown

We quantify the mechanisms controlling the CO_2 drawdown by expanding an existing ocean pCO_2 decomposition framework to include all contributions from physical (advection, mixing, freshwater, and thermal fluxes) and biological (photosynthesis and remineralization) processes. This framework focuses on the surface ocean pCO_2 budget because it is the main source of air-sea CO_2 flux interannual variability in the tropical Pacific Ocean (Doney et al., 2009; McKinley, Follows, et al., 2004; Obata & Kitamura, 2003). In our model, temporal variations in the air-sea CO_2 partial pressure difference ($\Delta pCO_2 = pCO_{2w} - pCO_{2a}$) explains 92% of the FCO_2 interannual variance in the tropical Pacific Ocean (we used a linear Taylor expansion of Equation 1 to isolate the effect of ΔpCO_2 interannual variations from the effect of wind, see Doney et al., 2009 for details on this approach). Furthermore, we find that variations in pCO_{2w} accounted for 95.4% of the ΔpCO_2 variance in the tropical Pacific Ocean, while pCO_{2a} only accounted for 2%. This is consistent with the fact that the ocean surface pCO_2 variability on interannual time scale can be up to 100 times larger than the atmospheric CO_2 variability.

Our starting point is the traditional approach that link variations in ocean pCO_2 (pCO_{2w}) to changes in DIC, Alk, temperature, and salinity using the following linear decomposition (Le Quéré et al., 2000; Takahashi et al., 1993):

$$\Delta pCO_{2w} \approx \frac{\partial pCO_{2w}}{\partial DIC}\Delta DIC + \frac{\partial pCO_{2w}}{\partial Alk}\Delta Alk + \frac{\partial pCO_{2w}}{\partial T}\Delta T + \frac{\partial pCO_{2w}}{\partial S}\Delta S \tag{2}$$

where T and S denote ocean water temperature and salinity, respectively. Using this approach, past studies have identified DIC as the main driver of pCO_2 interannual variability in the tropical Pacific Ocean and then used model results to quantify the physical and biological processes that ultimately control DIC (e.g., Doney et al., 2009; Le Quéré et al., 2000). This approach is however limited because it considers only one of the drivers of pCO_2 (i.e., DIC) and ignores how covariations in DIC, Alk, temperature, and salinity can dampen or reinforce each other.

We expand this method to consider the effect of the four tracers. Using the linear decomposition of Equation 2 here and referring to Equation 5 in Le Quéré et al. (2000), we can express the temporal change in pCO_{2w} (units: uatm/s) as a function of the temporal changes in DIC, Alk, temperature, and salinity:

$$\partial_t pCO_{2w} \approx \frac{\partial pCO_{2w}}{\partial DIC}\partial_t DIC + \frac{\partial pCO_{2w}}{\partial Alk}\partial_t Alk + \frac{\partial pCO_{2w}}{\partial T}\partial_t T + \frac{\partial pCO_{2w}}{\partial S}\partial_t S \tag{3}$$

Temporal changes in DIC, Alk, T, and S are controlled by ocean transport, biological processes and air sea fluxes as follows:

$$\partial_t DIC \approx \partial_t DIC_H + \partial_t DIC_V + \partial_t DIC_{FCO_2} + \partial_t DIC_{Bio} + \partial_t DIC_{FW} \tag{4}$$

$$\partial_t Alk \approx \partial_t Alk_H + \partial_t Alk_V + \partial_t Alk_{Bio} + \partial_t Alk_{FW} \tag{5}$$

$$\partial_t T \approx \partial_t T_H + \partial_t T_V + \partial_t T_Q \tag{6}$$

$$\partial_t S \approx \partial_t S_H + \partial_t S_V + \partial_t S_{FW} \tag{7}$$

where the subscript H denotes the contribution from horizontal transport (advection and diffusivity in the meridional and zonal directions), V denotes the contribution from vertical transport (vertical advection and diffusivity), *Bio* denotes the DIC and Alk changes induced by biological processes (photosynthesis, respiration, calcium carbonate dissolution/precipitation, denitrification, and nitrification), Q denotes the effect of surface heat flux, *FW* denotes the effect of freshwater fluxes (i.e., precipitation, evaporation, river, and sea ice melt), and $\partial_t DIC_{FCO_2}$ denotes the DIC change induced by air-sea CO_2 flux.

Combining Equations 3–7 yields the following:

$$\begin{aligned}\partial_t pCO_{2w} \approx & \frac{\partial pCO_{2w}}{\partial DIC}(\partial_t DIC_H + \partial_t DIC_V + \partial_t DIC_{FCO_2} + \partial_t DIC_{Bio} + \partial_t DIC_{FW}) \\ & + \frac{\partial pCO_{2w}}{\partial Alk}(\partial_t Alk_H + \partial_t Alk_V + \partial_t Alk_{Bio} + \partial_t Alk_{FW}) \\ & + \frac{\partial pCO_{2w}}{\partial T}(\partial_t T_H + \partial_t T_V + \partial_t T_Q) + \frac{\partial pCO_{2w}}{\partial S}(\partial_t S_H + \partial_t S_V + \partial_t S_{FW})\end{aligned} \tag{8}$$

We rearrange the terms of Equation 8 (units: uatm/s) to isolate the temporal changes in pCO_{2w} (time tendency referred to as the pCO_2 *change*) and the influence of the air-sea CO_2 flux on pCO_{2w} (referred to as the *flux response*) on the left-hand side (LHS), and the five terms that control this pCO_2 and flux responses on the right-hand side (RHS):

$$\begin{aligned}&\underbrace{\left(-\frac{\partial pCO_{2w}}{\partial DIC}\partial_t DIC_{FCO_2}\right)}_{Flux\ response} + \underbrace{(\partial_t pCO_{2w})}_{pCO_2\ change} \\ &\approx \underbrace{\left(\frac{\partial pCO_{2w}}{\partial DIC}\partial_t DIC_H + \frac{\partial pCO_{2w}}{\partial Alk}\partial_t Alk_H + \frac{\partial pCO_{2w}}{\partial S}\partial_t S_H\right)}_{H_{Circ}} \\ &+ \underbrace{\left(\frac{\partial pCO_{2w}}{\partial DIC}\partial_t DIC_V + \frac{\partial pCO_{2w}}{\partial Alk}\partial_t Alk_V + \frac{\partial pCO_{2w}}{\partial S}\partial_t S_V\right)}_{V_{Circ}} \\ &+ \underbrace{\left(\frac{\partial pCO_{2w}}{\partial DIC}\partial_t DIC_{FW} + \frac{\partial pCO_{2w}}{\partial Alk}\partial_t Alk_{FW} + \frac{\partial pCO_{2w}}{\partial S}\partial_t S_{FW}\right)}_{FW} \\ &+ \underbrace{\left(\frac{\partial pCO_{2w}}{\partial DIC}\partial_t DIC_{Bio} + \frac{\partial pCO_{2w}}{\partial Alk}\partial_t Alk_{Bio}\right)}_{Bio} + \underbrace{\left(\frac{\partial pCO_{2w}}{\partial T}(\partial_t T_H + \partial_t T_V + \partial_t T_Q)\right)}_{Thermal}\end{aligned} \tag{9}$$

The five terms (units: uatm/s) on the RHS are the horizontal and vertical transport of dissolved species, that is, DIC, Alk and salinity (H_{Circ} and V_{Circ}), the dilution/concentration effect induced by freshwater fluxes and evaporation (*FW*), the biological effect due to photosynthesis, respiration, calcium carbonate dissolution/precipitation, denitrification, and nitrification (*Bio*), and vertical and horizontal transport and air-sea flux of heat (*Thermal*). Positive physical and biological contributions on the RHS would yield an increase in pCO_2 (positive pCO_2 change on LHS) and an oceanic outgassing of CO_2 acting to balance this increase in ocean pCO_2 (positive flux response on LHS).

The coefficients used for the pCO_{2w} dependence on DIC, Alkalinity, temperature, and salinity are approximated by the following equations (Lovenduski et al., 2007; Sarmiento & Gruber, 2006):

$$\frac{\partial pCO_{2w}}{\partial DIC} \approx \frac{\overline{pCO_{2w}}}{\overline{DIC}} \frac{3 \times \overline{Alk} \times \overline{DIC} - 2 \times \overline{DIC}^2}{(2 \times \overline{DIC} - \overline{Alk})(\overline{Alk} - \overline{DIC})} \tag{10}$$

$$\frac{\partial pCO_{2w}}{\partial Alk} \approx -\frac{\overline{pCO_{2w}}}{\overline{Alk}} \frac{\overline{Alk}^2}{(2 \times \overline{DIC} - \overline{Alk})(\overline{Alk} - \overline{DIC})} \tag{11}$$

$$\frac{\partial pCO_{2w}}{\partial T} \approx \overline{pCO_{2w}} \times 0.0423 \tag{12}$$

$$\frac{\partial pCO_{2w}}{\partial S} \approx \frac{\overline{pCO_{2w}}}{\overline{S}} \tag{13}$$

where overbar denotes 1982–2017 annual means. The coefficients are time invariant. Coefficients for DIC and salinity (Equations 10 and 13) are positive, that is, pCO_{2w} increases with DIC and salinity, while the

coefficient for alkalinity (Equation 11) is negative, that is, pCO_{2w} decreases with increasing alkalinity. The effects of DIC and Alk are often competing in changing pCO_{2w}, but the DIC effect generally dominates because the absolute value of the DIC coefficient is larger than the alkalinity coefficient in most regions of the ocean including the tropical Pacific Ocean (Doney et al., 2009; Le Quéré et al., 2000; Takahashi et al., 1993). However, in some anomalous cases the change in alkalinity can overcome the change in DIC. For example, when both DIC and Alk are diluted by precipitation at the surface, the air-sea CO_2 flux will act to compensate for the change in DIC but will not affect the change in Alk. As a result, the anomalous vertical Alk gradient can exceed the anomalous vertical DIC gradient and therefore control the influence of the anomalous vertical dynamic term (V_{Circ}).

2.5. Mixed-Layer Budget During the Anomalous CO_2 Drawdown Period

We quantify the contribution of the different biological and physical processes to the temporal changes in pCO_{2w} (pCO_2 change) and the air-sea CO_2 (flux response) using the pCO_2 budget of Equation 9 averaged between the surface and the mixed layer depth (depth where the water density is 0.01 kg/m^3 denser than the water at the surface) and integrated in time between the onset and the peak of the ocean CO_2 drawdown. This onset-to-peak period is key because it corresponds to the period when the ocean physics and biology are actively driving the CO_2 drawdown, for instance, by reducing the supply of DIC to the surface. Figure S4 illustrates how the onset, peak, and duration of the anomalous CO_2 drawdown associated with El Niño events across the tropical Pacific Ocean. At each point, the peak time (t_{peak}) is the month when the CO_2 flux interannual anomaly is minimum between October of Year(0) and December of Year(+1), and the onset (t_{onset}) is the month when the anomaly becomes negative prior to the peak time in Year(0) (see Figure S4). Note that if the CO_2 flux anomaly does not cross zero in Year(0), we assume t_{onset} is January of Year(0). This yields (units: uatm)

$$\underbrace{\int_{t_{onset}}^{t_{peak}}\left(-\frac{\partial pCO_{2w}}{\partial DIC}\partial_t DIC_{FCO_2}\right)\mathrm{d}t}_{Flux\ response}+\underbrace{\int_{t_{onset}}^{t_{peak}}(\partial_t pCO_{2w})\mathrm{d}t}_{pCO_2\ change}$$
$$\approx\underbrace{\int_{t_{onset}}^{t_{peak}}\left(\frac{\partial pCO_{2w}}{\partial DIC}\partial_t DIC_H+\frac{\partial pCO_{2w}}{\partial Alk}\partial_t Alk_H+\frac{\partial pCO_{2w}}{\partial S}\partial_t S_H\right)\mathrm{d}t}_{H_{Circ}}$$
$$+\underbrace{\int_{t_{onset}}^{t_{peak}}\left(\frac{\partial pCO_{2w}}{\partial DIC}\partial_t DIC_V+\frac{\partial pCO_{2w}}{\partial Alk}\partial_t Alk_V+\frac{\partial pCO_{2w}}{\partial S}\partial_t S_V\right)\mathrm{d}t}_{V_{Circ}}$$
$$+\underbrace{\int_{t_{onset}}^{t_{peak}}\left(\frac{\partial pCO_{2w}}{\partial DIC}\partial_t DIC_{FW}+\frac{\partial pCO_{2w}}{\partial Alk}\partial_t Alk_{FW}+\frac{\partial pCO_{2w}}{\partial S}\partial_t S_{FW}\right)\mathrm{d}t}_{FW}$$
$$+\underbrace{\int_{t_{onset}}^{t_{peak}}\left(\frac{\partial pCO_{2w}}{\partial DIC}\partial_t DIC_{Bio}+\frac{\partial pCO_{2w}}{\partial Alk}\partial_t Alk_{Bio}\right)\mathrm{d}t}_{Bio}+\underbrace{\int_{t_{onset}}^{t_{peak}}\left(\frac{\partial pCO_{2w}}{\partial T}(\partial_t T_H+\partial_t T_V+\partial_t T_Q)\right)\mathrm{d}t}_{Thermal} \quad (14)$$

Note that the difference between the LHS and RHS of Equation 14, which arises from the linearization of pCO_2 (Equation 2) is very small and negligible (see Figures 5 and S9).

2.6. Atmospheric Transport Model

We used the GEOS-Chem atmospheric transport model to evaluate the influence of the ocean CO_2 drawdown on atmospheric CO_2 (Nassar et al., 2010, 2011) as part of the NASA Carbon Monitoring System Flux (CMS-Flux) project (Bowman et al., 2017; Liu et al., 2014, 2017). GEOS-Chem is a global chemical transport model driven by operational analysis or reanalysis meteorological fields. We use GEOS-Chem transport model to simulate 3-hourly CO_2 concentrations with the hindcast air-sea CO_2 fluxes as boundary conditions between 1992 and 2018. CO_2 is transported as a passive tracer (i.e., no chemical reactions). In order to isolate the atmospheric tracer of ocean carbon flux, we only use the air-sea CO_2 fluxes derived from the ocean model MOM6 in the transport simulations. We run GEOS-Chem transport model at 2° × 2.5° spatial resolution

with 47 vertical layers with the top at 0.01 hPa. The atmospheric model is driven by MERRA2 reanalysis (Gelaro et al., 2017). We computed the column-integrated atmospheric CO_2 mole fraction (XCO_2) interannual anomaly in 1998 and 2016 a similar approach as in Chatterjee et al. (2017). We deseasonalized and detrended the monthly XCO_2 time series obtained with GEOS-Chem by first removing the 7-year monthly linear trend (one trend is computed for each month independently) and correct for the global background increase in atmospheric CO_2 by removing the global mean monthly XCO_2. Note that the 7-year monthly linear trends are computed using the 1994–2000 period for the 1998 event and the 2012–2017 period for the 2016 event.

3. Results

In this section, we first examine the observed and simulated spatial and temporal response to El Niño events (section 3.1), then analyze the mechanisms controlling the mean response to El Niño events using a composite of six events (section 3.2), and finally examine how these mechanisms and the associated response can vary between extreme eastern Pacific and moderate central Pacific El Niño events (section 3.3).

3.1. Observed and Simulated Response to El Niño Events

3.1.1. East–West Contrast in the Equatorial Region

We compare key characteristics of El Niño events in the observations and the model using moorings that capture the east–west equatorial gradient between the edge of the warm pool in the west central Pacific (average of three moorings located at 190°E to 2°S, 0°N and 2°N) and the equatorial upwelling which intensifies from the east central Pacific (one mooring at 220°E, 0°N) to the east Pacific (one mooring at 250°E, 0°N, Figures S5 and S6).

The model reproduces the amplitude of the surface warming and the eastward deepening of the thermocline that follows the strong westerly wind burst anomalies observed in the central equatorial Pacific (Figure S5). The model also captures the contrast between moderate central Pacific events, in which warm water (SST $\geq$ 30°C), heavy rainfall ($\geq$10 mm/day), and surface freshening are confined to the central equatorial Pacific west of 190°E (e.g., 2002/2003 and 2015/2016), and extreme eastern Pacific events when warm water, heavy rainfall, and surface freshening extend into the eastern Pacific as far as 250°E (e.g., 1982/1983 and 1997/1998, Figures S5 and S6). We note that the model tends to overestimate the amplitude of the freshening, probably due to the too shallow equatorial mixed-layer that reinforces the effect of precipitation on SSS (Figure S1).

These physical changes are associated with changes in the ocean-atmosphere pCO_2 difference (ΔpCO_2). Observations at the TAO moorings show that ΔpCO_2 drops by 25–100 uatm during El Niño events, with the most intense changes occurring at 250°E (Figure S6). The model reproduces the changes observed at these moorings although it slightly underestimates their magnitude (by about 30 uatm, Figure S6). The wind speed (JRA55-do v1.3) used to force the model and compute the CO_2 flux tracks very well ($r^2 = 0.82$) the zonal wind speed measured at TAO moorings (see Figures S5d–S5f) suggesting that wind is a weak source of bias in the simulated CO_2 flux (Taboada et al., 2019). The bias in the flux anomaly is likely tied to the shallow equatorial mixed-layer and strong stratification which reduce the upward mixing of high pCO_2 waters. During extreme events (e.g., 1997/1998), the ΔpCO_2 is close to equilibrium in both observations and model in the central equatorial Pacific. These mooring data provide invaluable in situ constraints on the physical and pCO_2 response associated with El Niño events in the equatorial region. Yet to understand the full extent of the ocean CO_2 drawdown and its influence on atmospheric CO_2, we need to expand the analysis and consider the temporal and spatial evolution of the oceanic response at the basin scale.

3.1.2. Basin-Scale Pattern, Timing, and Magnitude of Anomalous Ocean CO_2 Drawdown

The reduced CO_2 outgassing associated with El Niño events covers the central and eastern equatorial Pacific but also extends poleward into the tropical Pacific Ocean. Figure 2 shows the spatial air-sea CO_2 flux composite response associated with six El Niño events in two pCO_2 observation-based products (MLS and SOM-FFN, Landschützer et al., 2014; Rödenbeck et al., 2013). The tropical air-sea CO_2 flux anomaly is most intense in a band that extends from the north central Pacific (5°S to 20°N; 160–180°E) to the southeast Pacific (15°S to 0°N; 240–290°E) (Figure 2). The two pCO_2-based products suggest that, in this north central

to southeast band, the ocean source of CO_2 to the atmosphere is reduced by 1 to 8 $gC/m^2/yr$ which corresponds to a decrease of 10–30% (compared to the climatological source of 10–30 $gC/m^2/yr$, Figure S3).

The anomalous CO_2 drawdown averaged over the tropical Pacific Ocean (15°S to 15°N) lasts for about 2 years between boreal Spring of Year(0) and Year(+2) (Figure 2). The two pCO_2 observation-based products suggest that the CO_2 flux anomaly was 2 to 4 times larger during the events of 1997/1998 and 2015/2016 (−0.40 to −0.30 PgC/yr) than during the moderate event of 2002/2003 (−0.20 to 0.0 PgC/yr). However, the two products differ by more than a factor 2 in the magnitude of the flux anomaly in certain years (e.g., −0.20 PgC/yr in MLS vs. -0.05 PgC/yr in SOM-FFN in 2002/2003) and in the composite mean response (−0.25 PgC/yr in MLS vs. −0.10 PgC/yr in SOM-FFN). These differences can be attributed to differences in the CO_2 flux anomaly in the north central Pacific and in the eastern equatorial Pacific (Figure 2) where the pCO_2 data coverage is probably insufficient to capture the interannual variability associated with El Niño events. These differences in the magnitude are also associated with differences in the timing of the CO_2 flux anomaly. The CO_2 flux anomaly onsets before the Niño3.4 index peaks in both products and in agreement with direct in situ observations (e.g., Sutton, Feely, et al., 2014). However, the flux anomaly is most strongly correlated to the Niño3.4 index without any time lag in the SOM-FFN product ($r^2 = 0.44$ at 0 lag) but with a 3-month lag in the MLS product (CO_2 flux negative anomaly peaks 3 months after the Niño3.4 index, $r^2 = 0.24$ at 0 lag and 0.34 at 3-month lag). The stronger correlation in the SOM-FFN product is likely related to the interpolation method that heavily depends on SST. Prior studies have shown that the pCO_2-based MLS product has the lowest relative interannual variability mismatch ratio in the equatorial Pacific, which suggests that it may better capture the temporal changes associated with interannual variability and El Niño events in this region (see R^{IAV} in Denvil-Sommer et al., 2019 and Rödenbeck et al., 2015).

The ocean model largely reproduces the magnitude, spatial distribution, and temporal evolution of the CO_2 flux anomaly expected from the data-based composite mean. The model simulates the 2-year duration of the CO_2 anomaly and the band of intense flux anomaly (−1 to −8 $gC/m^2/yr$) that extends from the north central to southeast Pacific (Figure 2). The main data-model mismatch is the stronger drawdown simulated in the southeast tropical Pacific and along the Peruvian coast (Figure 2). A strong reduction of the ocean CO_2 source associated with the coastal upwelling and offshore advection is expected in this region, but the model might misrepresent these processes due to its relatively coarse horizontal resolution (0.5°). Yet because pCO_2 is poorly sampled by observations in this region, it is difficult to assess how much of this mismatch is attributable to a model bias or to data scarcity. We also note that in the model the six-event composite the weakened CO_2 outgassing lasts longer in boreal Summer of Year(+1). As we discuss later, this is likely due to the strong contribution from the 1997/1998 El Niño event where the flux anomaly persisted into boreal Summer.

3.1.3. Anomalous CO_2 Drawdown From Onset to Peak Time

The anomalous CO_2 drawdown onsets (flux anomaly becomes negative) and peaks (flux anomaly minimum) at different times depending on the location (Figure 3). The pCO_2-based data products and model composite indicate that the CO_2 flux anomaly onset starts in the central equatorial Pacific (January–February Year(0)) and then progresses to the eastern equatorial Pacific and poleward to the southern and northern tropical Pacific (onset in March–November Year(0)). The CO_2 flux anomaly tends to peak earlier in the central and northern tropical Pacific (December–February Year(+1)) than in the eastern and southern tropical Pacific (January–December Year(+1)). The data products and model results are consistent in this large scale pattern but show some local differences, specifically in the eastern Pacific (e.g., later onset in pCO_2-based SOM-FFN and earlier peak time in pCO_2-based MLS; note that regions that peak after June are located around 200°E in pCO_2-based MLS, but around 240°E in pCO_2-based SOM-FFN). Some of these differences are attributable to the onset and peak detection method, for instance, when the signal presents several consecutive peaks of similar magnitude.

This period between onset and peak is crucial because it corresponds to the period when the ocean physics and biology are active in driving and reinforcing the CO_2 flux response. In contrast, after the peak, these physical and biological drivers are weakening and unable to sustain the anomalous air-sea CO_2 flux, which gradually returns to its climatological value. In the following, we use this period to examine the processes controlling the CO_2 response.

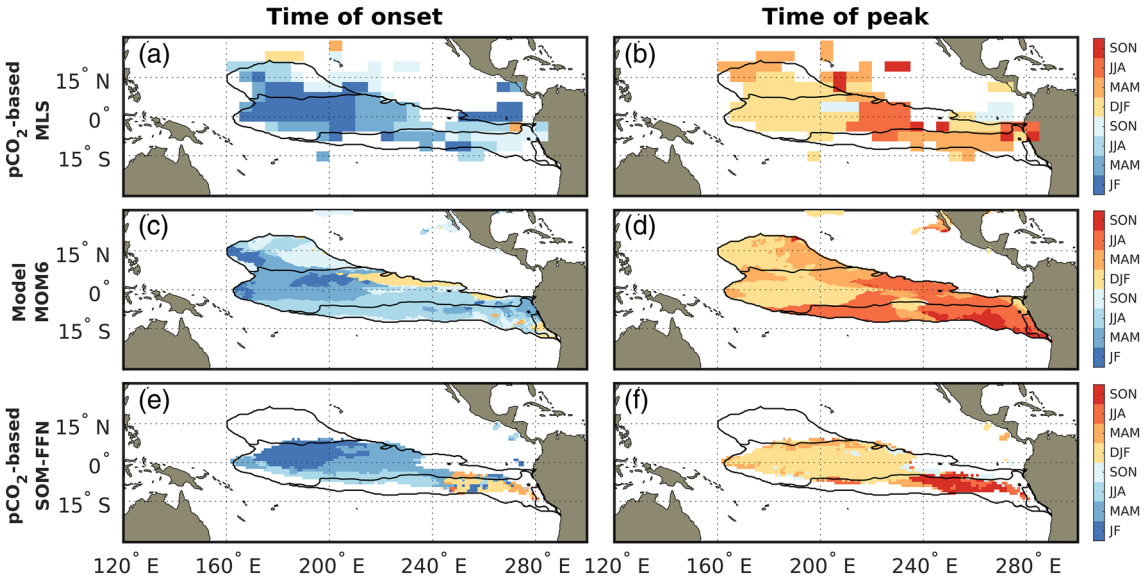

Figure 3. Observed and simulated (a, c, and e) onset and (b, d, and f) peak times of the CO_2 flux composite anomaly in the region of intense CO_2 drawdown (< -1.6 gC/m^2/yr, see Figure 2). At onset, the flux anomaly becomes negative and at peak time, the flux anomaly is minimum. Year(0) is in cold colors, Year(+1) in warm colors. Observational pCO_2-based products are from Rödenbeck et al. (2013) mixed-layer scheme (MLS, a-b) and Landschützer et al. (2014) neural network interpolation (SOM-FFN, e-f). The composite includes six El Niño events. Black contours delimit the three regions of anomalous CO_2 drawdown simulated by the model (see near-equatorial, southern, and northern on Figure 5). See section 2 for details on onset and peak times.

3.2. Mechanisms Controlling the CO_2 Response Spatial and Temporal Evolution

3.2.1. Three Regions Controlled by Different Mechanisms

We examine what physical and biological processes control the integrated change in pCO_2 (pCO_2 time tendency) and the air-sea CO_2 flux response (change in pCO_2 that has been compensated by an air-sea CO_2 flux) in the mixed-layer between the onset and peak times in the model (Equation 14 and Figure 4). Physical and biological processes include freshwater fluxes (e.g., dilution/concentration effect), vertical and horizontal transport of chemical species (e.g., advection, diffusivity and mixing of DIC, Alkalinity, and salinity), biological uptake and drawdown of DIC and Alkalinity, and thermal fluxes associated with ocean circulation and air-sea heat fluxes (see methods in sections 2.4 and 2.5).

The cumulative change in pCO_2 between the onset and peak times is relatively homogeneous spatially in the region of anomalous drawdown (less than −30 uatm in most areas Figure 4b). In contrast, the air-sea flux response ranges from −120 uatm in the equatorial and Peruvian upwelling regions to −30 uatm in the northern and southern regions flanking the equator (Figure 4a). We define three subregions based on the mechanisms that control the strong negative anomalies in the pCO_2 and air-sea flux responses (Figures 4 and 5a):

1. the “near-equatorial drawdown region” where the pCO_2 and flux responses are controlled by changes in *vertical transport and rainfall* (e.g., dilution effect). This region encompasses the equatorial band east of 160°E (eastern edge of the warm pool and equatorial upwelling), the northern and southern flanks of this equatorial band (up to 8° of latitude). It also includes the Peruvian coastal upwelling, which is not strictly a “near-equatorial” region but contributes little compared to the rest of the region.
2. the “southern drawdown region” and “northern drawdown region”, respectively, located in the southeast tropical Pacific (200–280°E, 5–10°S) and in the north central tropical Pacific (160–200°E, 5–20°N), and where the pCO_2 and flux responses are dominated by changes in *horizontal transport*.

The near-equatorial region accounts for more than half of the anomalous CO_2 drawdown, while the northern and southern regions account for 20–40% (Figure 5b). The model suggests that the CO_2 flux anomaly first develops in the near-equatorial region in spring of Year(0) before propagating to the southern region in boreal fall and finally to the northern region in boreal winter (Figure 5b). Furthermore, the flux anomaly intensifies for about a year after its onset in the near-equatorial and southern regions, while it only intensifies for a few months after the onset in the northern region. As we show in the following this poleward propagation of

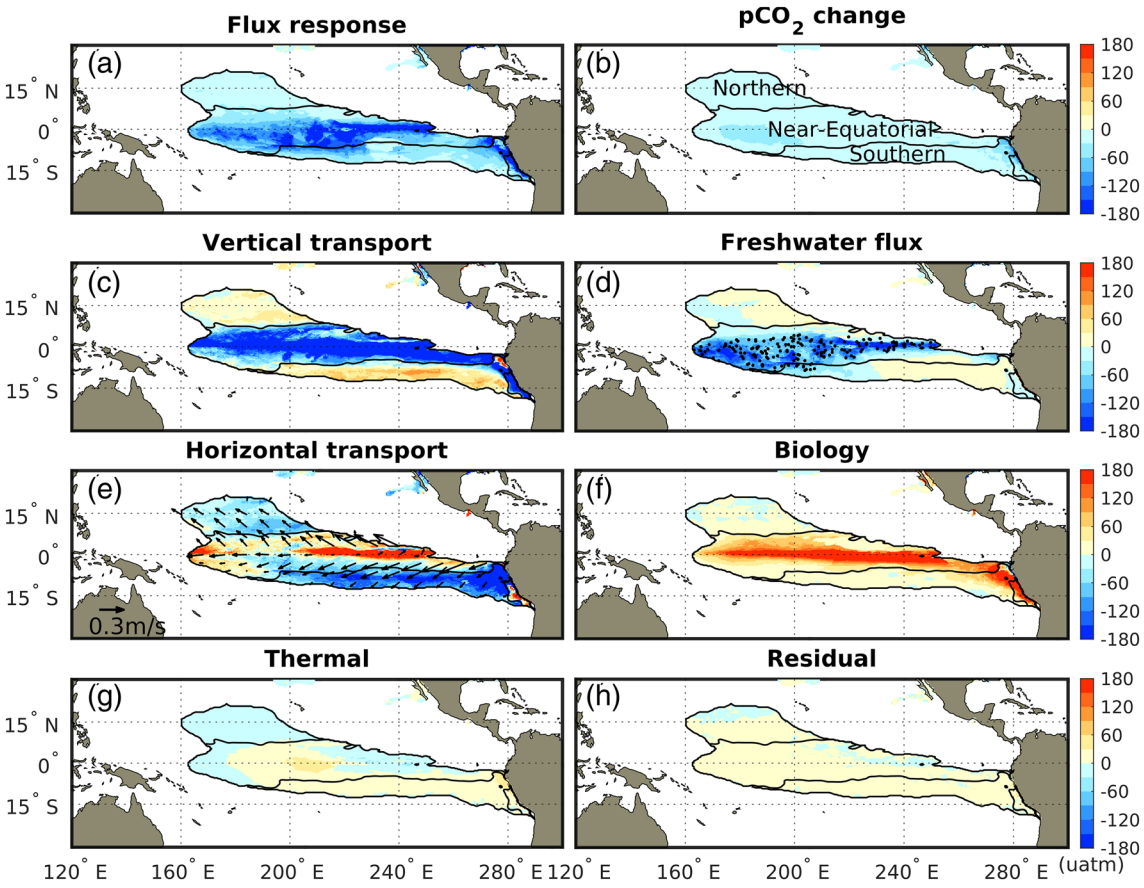

Figure 4. Processes controlling the composite response to El Niño in the model obtained from the mixed-layer budget integrated between the onset and peak times (in uatm, Equation 14). The onset-to-peak change in pCO_2 (b) and the flux response (a) (change in pCO_2 equilibrated by the air-sea flux) can be attributed to changes in vertical (c) and horizontal (e) transports, freshwater fluxes (d), biological activity (f), and thermal changes (g). The residual (h) shows the difference between the flux and pCO_2 change and the sum of the physical and biological contributions (h = (a + b) − (c + d + e + f), see Equation 14). Only the region of intense CO_2 drawdown is shown (<−1.6 gC/m^2/yr, see Figure 2). Black contours delimit the three regions defined in Figure 5. Currents in the mixed-layer (vectors in panel e) and rainfall anomaly larger than 2 mm/day (stippling in panel d) between December Year(0) and June Year(+1) are shown. Negative values correspond to a reduction in ocean pCO_2. See Figure 5 and Equation 14 in methods (section 2.5) for details on the mixed-layer budget.

the CO_2 drawdown is controlled by the horizontal transport of the pCO_2 anomaly originated in the near-equatorial region.

3.2.2. "Near-Equatorial" Drawdown Controlled by Rainfall and Vertical Transport

On average over the six El Niño events, the near-equatorial region covers 1.5×10^7 km^2 (Figure 5d). The combined pCO_2 tendency (pCO_2 change) and flux response averaged in this region amount to a decline in pCO_2 of 130 uatm between the onset and peak time. The primary controls of this pCO_2 decline are changes in vertical dynamics which account for a decrease in pCO_2 of 230 uatm between the onset and peak time and freshwater fluxes which further decrease pCO_2 by 60 uatm (Figures 4 and 5d).

Changes in freshwater fluxes during El Niño events are associated with the shift of intense convective rainfall from the western Pacific to the central equatorial Pacific and, in extreme cases like in 1997/1998, to the eastern equatorial Pacific (Figures S6 and S8; Dai & Wigley, 2000; Schneider et al., 2014). This anomalous freshwater flux dilutes surface DIC, alkalinity, and salinity and reduces pCO_2 in the mixed layer. This effect of freshwater flux is reinforced in the central Pacific by the eastward horizontal advection of fresh, DIC-poor/Alk-poor warm pool waters that reduces pCO_2 (2°S to 2°N, 160–200°E, Figure S7c). However, note that this effect is confined to the central Pacific and remains small compared to the total contribution of horizontal transport in the near-equatorial region which increases mixed-layer pCO_2 (see discussion on horizontal transport below, Figure 5d).

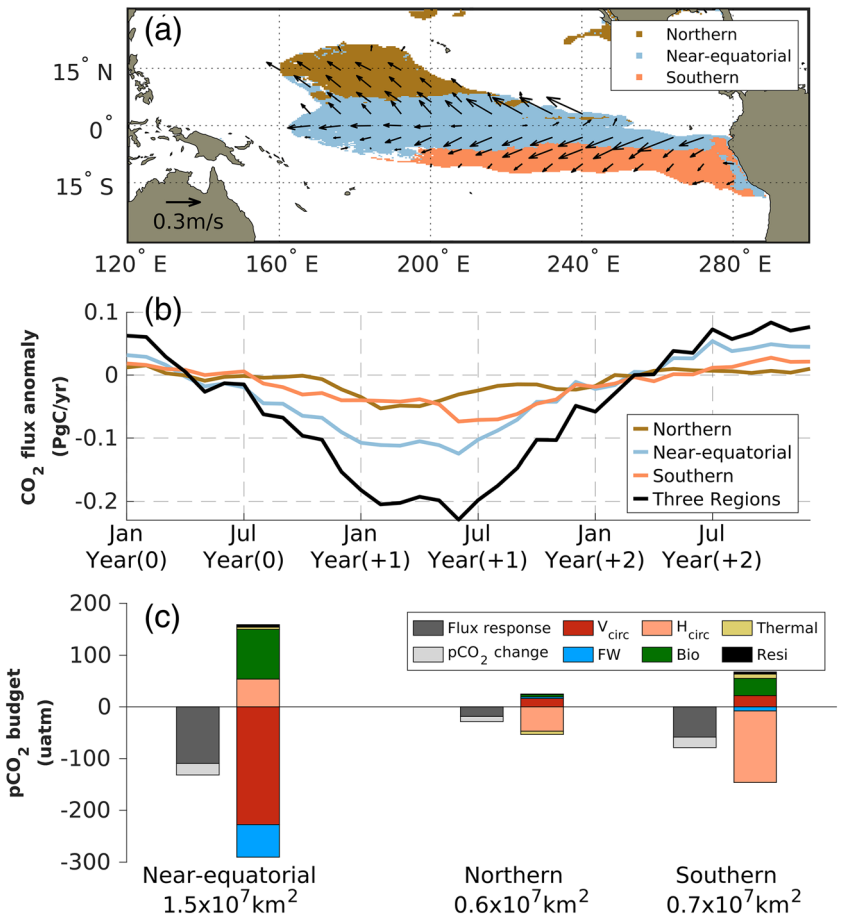

Figure 5. (a) Extent of the three regions of anomalous CO_2 drawdown (near-equatorial, northern, and southern) in the model composite response and currents in the mixed-layer averaged between December Year(0) to June Year(+1) (vectors); (b) CO_2 flux composite anomaly integrated in the three regions; (c) mixed-layer pCO_2 budget integrated between onset and peak times and averaged in the three regions. The pCO_2 and flux responses can be attributed to vertical (V_{Circ}) and horizontal (H_{Circ}) transports, freshwater fluxes (FW), biological activity (bio), and thermal changes. The residual shows the difference between the sum of flux response and pCO_2 change and the sum of the physical and biological contributions (see Equation 14). Negative values correspond to a reduction in ocean pCO_2. See Figure 4 and Equation 14 in methods (section 2.5) for details on the mixed-layer budget.

The effect of vertical dynamics on pCO_2 is relatively complex. Prior work has shown that vertical advection and mixing are reduced during El Niño events because of (i) the weaker upwelling- and mixing-favorable winds and the deepening of the thermocline in the eastern Pacific and (ii) the increased stratification associated with anomalous rainfall and the eastward migration of the fresh warm pool in the central Pacific (e.g., Doney et al., 2009; Feely et al., 2002; McKinley, Follows, et al., 2004). Our model suggests that the vertical advection and mixing of DIC is only reduced in very limited areas of the eastern Pacific (east of 240°E) and along the northern equatorial flank where it indeed controls the decrease in mixed-layer pCO_2 (Figure 6a). This limited effect of reduced upwelling on DIC in the composite response is consistent with the fact that the equatorial wind stress and upwelling in the eastern Pacific only significantly recede during extreme eastern Pacific El Niños, such as in 1997/1998 when the intertropical convergence zone (ITCZ) was centered on the equator (Figures 1 and S8, Lengaigne & Vecchi, 2010; see more detail in the following section).

In contrast, the effect of vertical dynamics on pCO_2 in the central Pacific and along the equator (i.e., in most of the near-equatorial region) is tightly linked to changes in stratification. Vertical gradients in DIC, Alk, and salinity between the mixed layer and the subsurface intensify in response to the rainfall dilution effect and the eastward extension of warm pool waters (fresh, DIC- and Alk-poor waters advected on top of saltier,

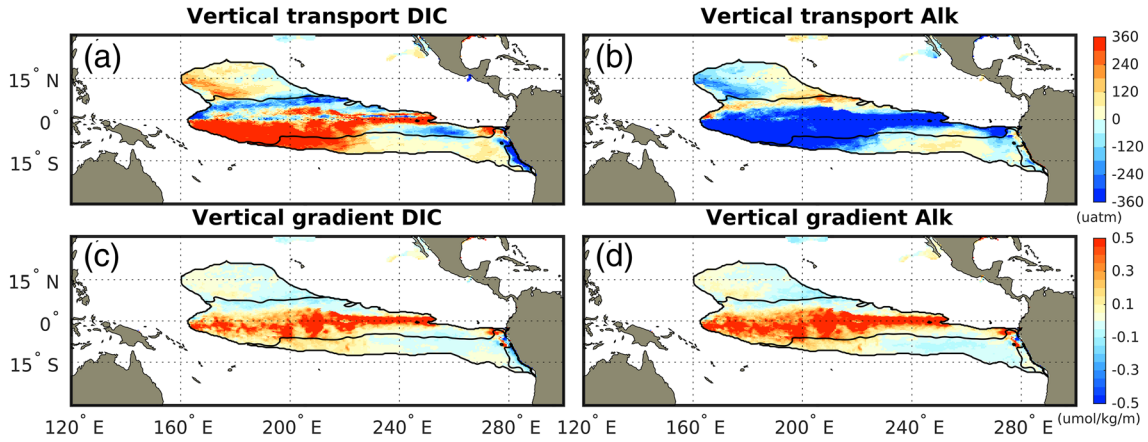

Figure 6. (a, b) Onset-to-peak time-integrated contributions from vertical transport of DIC and vertical transport of alkalinity to the composite response to El Niño. These contributions control the overall effect of vertical transport that also includes the vertical transport of salinity (Figure 4c). (c, d) Onset-to-peak time integrated change in the vertical gradients of DIC and alkalinity in the composite response to El Niño (vertical gradients are computed over the mixed-layer). Black contours delimit the three regions defined in Figure 5. See methods (section 2.5) for details on the mixed-layer budget.

DIC- and Alk-enriched waters, Figures 6c and 6d). The model suggests that this increase in vertical gradients overcomes the weakening in mixing and advection. The vertical transport of water is reduced but, perhaps counterintuitively, still increases the supply of DIC, Alk, and salinity to the mixed-layer (Figure 6). In this case, the effect of the anomalous Alk vertical gradient exceeds the effect of the anomalous DIC vertical gradient (probably because the air-sea CO_2 flux partly compensates the dilution of DIC but not the dilution of Alk). As a result, the pCO_2 in the mixed layer decreases (more supply of alkalinity reduces pCO_2, Figures 6a and 6b). We note that these model results on the response of the vertical dynamics are consistent with prior results which suggested that, despite reduced vertical advection and mixing, anomalous vertical supply from the subsurface actually increased salinity in the mixed,layer (Hasson et al., 2013).

The pCO_2 drawdown associated with vertical dynamics and rainfall dilution is partly balanced by the biological response and the horizontal transport which respectively accounts for an increase in mixed-layer pCO_2 of 100 uatm (offsets about 33%) and 50 uatm (offsets 18%) from onset to peak time (Figure 5d). The biological uptake of DIC and Alk in the mixed layer declines because of nutrient limitation (Chavez et al., 1999). The horizontal export of high pCO_2 waters drops (which appears as an anomalous increase in pCO_2) mainly because pCO_2 in the near-equatorial region drops. Finally, we find that the influence of thermal changes, which are associated with the transport of temperature by the ocean circulation and air-sea heat fluxes, are modest (<5 uatm, Figure 5d).

3.2.3. "Northern" and "Southern" Drawdown Regions Controlled by Horizontal Transport

The CO_2 flux anomaly extends from the near-equatorial region poleward into what we refer to as the southern and northern drawdown regions (Figure 4). Combined, the pCO_2 change (pCO_2 tendency) and flux response amount to a pCO_2 decline of 80 uatm in the southern region and 30 uatm in the northern region between the onset and peak time (Figures 5c and 5e). This decline in mixed-layer pCO_2 is controlled by reduced horizontal meridional transport (Figures 4e and S7), which alone accounts for a decrease in pCO_2 of 140 uatm in the southern region and 50 uatm in the northern region between onset and peak time (Figures 5c and 5e).

This effect of horizontal dynamics can be attributed to the weaker poleward Ekman transport of high pCO_2 waters from the near-equatorial region (Figures 4e and S7). As described previously, the pCO_2 in the near-equatorial region dramatically drops. The Ekman flow resulting from the equatorial trade winds is reduced during El Niño events, but it still transports and spreads out this low ocean pCO_2 anomaly from the near-equatorial region into the southern and northern drawdown regions (Figure S8). Notably, the effects of the southward and northward transport are characterized by a seasonal phase locking. The southward transport mostly exports the pCO_2 anomaly generated in the near-equatorial eastern Pacific (east of

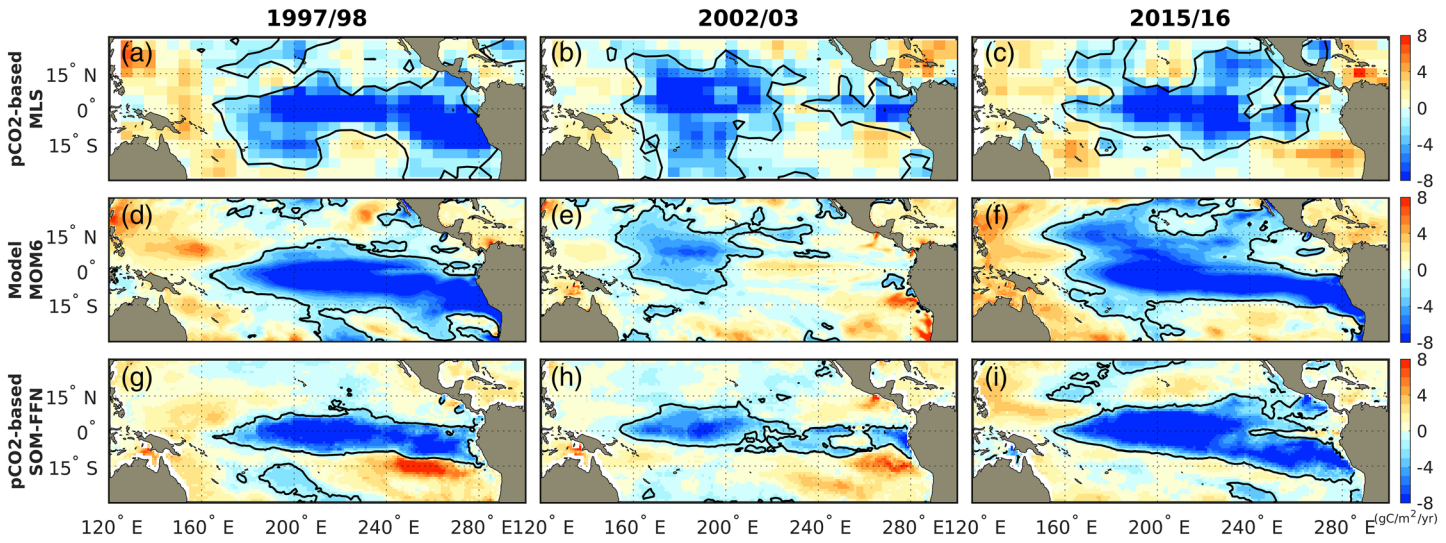

Figure 7. Observed and simulated air-sea CO_2 flux anomaly during the extreme east Pacific 1997/1998 (a, d, and g), moderate central Pacific 2002/2003 (b, e, and h), and strong central Pacific 2015/2016 (c, f, and i) El Niño events. Maps are 2-year averages from pCO_2-based products (SOM-FFN, Landschützer et al. (2014) and MLS, Rödenbeck et al., 2013) and the ocean model. Negative values are anomalous ocean uptake. Contours are flux anomaly of −1.6 gC/m^2/yr.

220°E) between boreal fall and spring (September of Year(0) to May of Year(+1), Figure S8), while the northward transport mostly exports the pCO_2 anomaly generated in the near-equatorial central Pacific (160–220°E) in boreal winter (December of Year(0) to February of Year(+1), Figure S8).

In both the southern and northern regions, changes in the Ekman transport also intensifies the vertical gradient between the anomalously low mixed-layer pCO_2 waters exported from the equatorial region and the high pCO_2 subsurface waters. As a result, vertical transport partially counteracts the effect of horizontal transport and increases pCO_2 by about 15–20 uatm between onset and peak time (Figures 5c and 5e). In the southern region, the decline in the biological uptake of DIC and Alk offshore the Peruvian upwelling also contributes to offset the pCO_2 drawdown (+30 uatm between onset and peak time, Figure 5e). Other terms (thermal and freshwater flux) have a much smaller influence (Figures 4 and 5).

3.3. Differences Between El Niño Events

We contrast three El Niño events: (i) the moderate central Pacific event of 2002/2003 (Niño 3.4 < 2°C); (ii) the strong central Pacific event of 2015/2016 (Niño 3.4 > 2°C), which combined eastern and central Pacific El Niño dynamics, but during which the central Pacific dynamics controlled the spatial extent and early termination (Paek et al., 2017); and (iii) the extreme eastern Pacific El Niño event of 1997/1998 during which the eastern equatorial upwelling collapsed because of the trade winds and southward displacement of the intertropical convergence zone (Niño 3.4 > 2°C and eastern equatorial wind stress anomaly < −0.02 N/m^2 Figure 1, e.g., Kao and Yu., 2009).

This comparison reveals considerable differences in the distribution and magnitude of the CO_2 flux anomaly in both observations and the model (Figure 7). The CO_2 flux anomaly in 2002/2003 ranged between −1.6 and −8 gC/m^2/yr and was principally confined to the central tropical Pacific (160–220°E), while it exceeded −8 gC/m^2/yr and covered most of the tropical Pacific Ocean east of 160°E during the 1997/1998 and 2015/2016 events. As a result, the simulated anomalous CO_2 drawdown during the moderate event was about 4 times weaker than during the other two events (Figure 8), which is consistent with the anomaly derived from the pCO_2-based products (Figure 2).

The three drawdown regions identified in the composite response (near-equatorial, southern, and northern) are present in all events, but differences in their area and the intensity of the processes controlling pCO_2 within them explain the differences in the CO_2 response at the basin scale. For instance, the CO_2 flux anomaly in the near-equatorial region was 2 to 4 times stronger in 1997/1998 than in 2002/2003 (Figure 8). This is explained by the stronger pCO_2 drawdown which was about 3 times stronger in 1997/1998 (pCO_2 change +

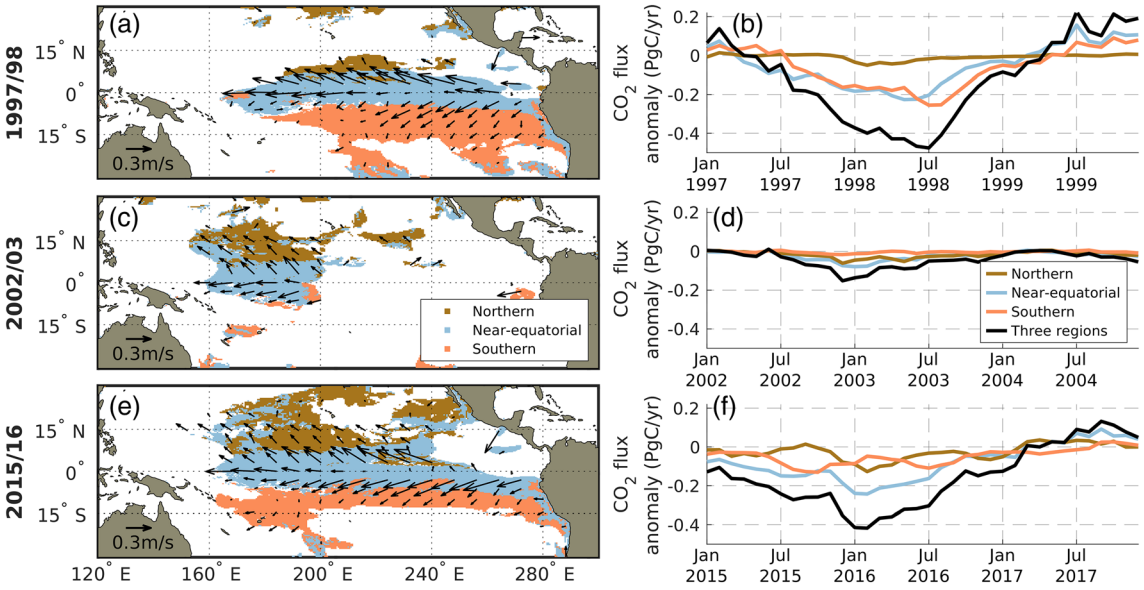

Figure 8. Extent of the three CO_2 drawdown regions (near-equatorial, northern, and southern regions) during the extreme east Pacific 1997/1998 (a), moderate Central Pacific 2002/2003 (c), and strong Central Pacific 2015/2016 (e) El Niño events and area-integrated CO_2 flux anomaly in the three regions (b, d, and f). Vectors are currents averaged in the mixed-layer between December Year(0) (1997, 2002, or 2015) and June Year(+1) (1998, 2003, or 2016).

flux response of 100 uatm vs. 300 uatm) but also by the 70% larger area of the near-equatorial region in 1997/1998 (1.7 vs. 1.0×10^7 km^2, Figure S9). Similarly, the combined pCO_2 drawdown of the southern and northern regions was about twice as strong in 1997/1998 than in 2002/2003 (pCO_2 change + flux response of 100 uatm vs. 200 uatm) and the total area of the two regions was more than doubled (2.0 vs. 0.9×10^7 km^2).

The CO_2 flux anomaly during the eastern Pacific event of 1997/1998 differs from the other two events and the composite response because it persisted well into boreal spring and summer, while other El Niño events usually recedes in boreal winter/early-spring (Figures 8 and 5). The CO_2 flux anomaly peaked 5 to 7 months later in 1997/1998 (July 1998) than in 2015/2016 (February 2016) and 2002/2003 (December 2002). In addition, the flux anomaly extended much further south in the case of 1997/1998, while it extended much further north in 2002/2003 and 2015/2016 (Figures 7 and 8). These differences ensue from the spatiotemporal evolution of the pCO_2 anomaly in the near-equatorial region and how it is subsequently amplified by poleward Ekman transport. The comparison of 1997/1998 and 2015/2016 is insightful here because both events were strong (Niño 3.4 > 2°C, average CO_2 flux anomaly >8 gC/m^2/yr), but the upwelling only collapsed during the extreme case of 1997/1998 when the ITCZ was centered on the eastern equatorial Pacific (Figure S10). As a result, the near-equatorial pCO_2 anomaly intensified until the end of boreal spring 1998 and was particularly strong in the southeastern Pacific (Figure S11). This long-lasting near-equatorial pCO_2 anomalies in the south–east enabled a vigorous southward Ekman transport of the pCO_2 anomaly that lasted from summer 1997 to summer 1998. In contrast, in 2015/2016 the ITCZ remained in the Northern Hemisphere, westerly winds anomalies (Figure S10); the near-equatorial pCO_2 anomaly was weaker, mostly located in the central Pacific and it subsided at the end of boreal winter 2016 (Figure S11). The short-lived near-equatorial pCO_2 anomalies tapered off the CO_2 flux anomaly in 2016, but it was still active and accessible to the boreal winter northward Ekman transport (Figures 7 and 8).

3.4. Influence on Atmospheric CO_2

We evaluate how differences in the magnitude and spatiotemporal evolution of the air-sea CO_2 flux between events influence atmospheric CO_2 and discuss in section 4 whether satellite observations of atmospheric CO_2 could detect these differences and provide basin-scale constraints on the ocean response. We compare the atmospheric CO_2 anomaly expected from the ocean response during the El Niño events of 1997/1998 and 2015/2016 (Figure 9). We obtained the atmospheric anomalies by transporting the ocean CO_2 flux with the

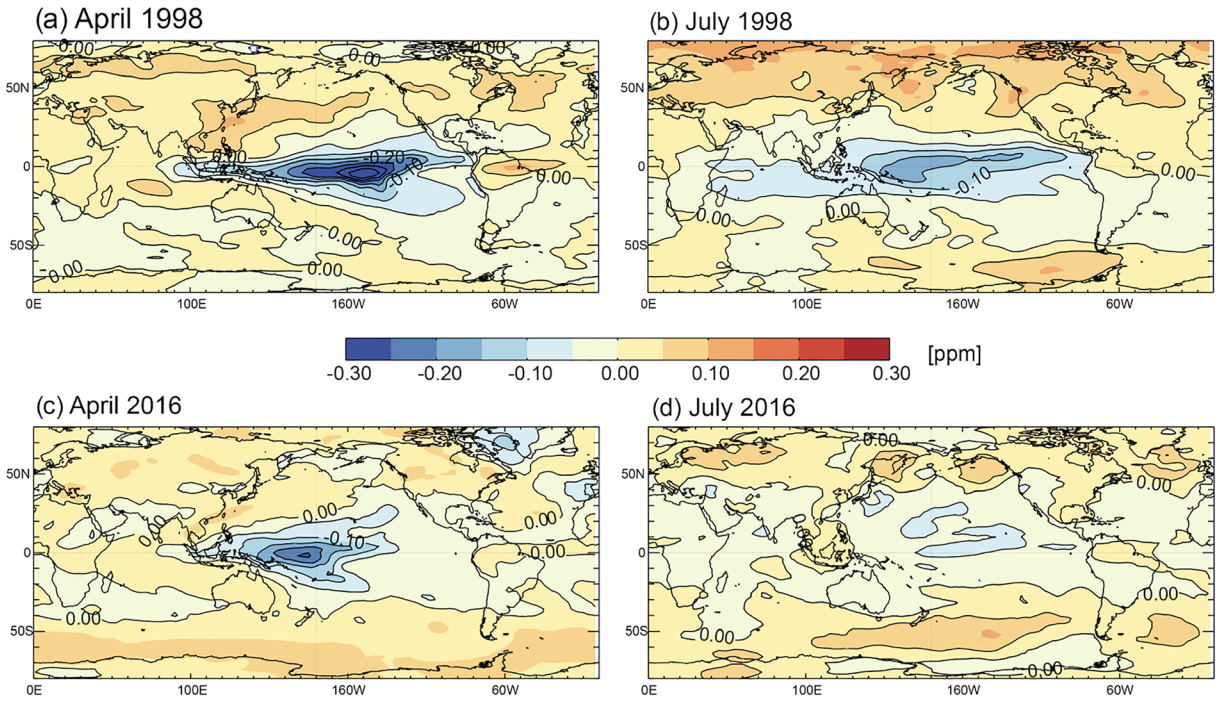

Figure 9. Atmospheric CO_2 drawdown (in ppm) induced by the oceanic CO_2 flux anomaly in (a) April and (b) July of 1998 and (c) April and (d) July of 2016. This is obtained by transporting the air-sea CO_2 flux from the ocean model using the GEOS-CHEM atmospheric transport model. See details in methods (section 2.6).

GEOS-Chem atmospheric transport model used in CMS-Flux (see methods in section 2.6). Note that Figure 9 includes the effects of air-sea flux and atmospheric transport anomalies but exclude other effects such as the net reduced uptake by the land biosphere.

In both 1997/1998 and 2015/2016, the atmospheric anomaly was shifted westward compared to the ocean flux anomaly due to the transport by trade winds. We find, however, that differences in the air-sea flux anomaly influences the magnitude, distribution, and duration of the atmospheric anomaly. The prolonged and intense anomalous ocean CO_2 drawdown during the 1997/1998 event caused a pronounced basin-wide negative anomaly in atmospheric CO_2 that peaked in the central Pacific in boreal spring of 1998 (−0.35 ppm) and persisted into boreal summer of 1998 (Figures 9a and 9b). In contrast, the flux anomaly during the 2015/2016 event yielded a weaker atmospheric CO_2 negative anomaly (−0.25 ppm) largely confined to the western Pacific Ocean and to boreal spring in 2016 (Figures 9c and 9d).

4. Discussion and Conclusion

The reduction of the ocean CO_2 outgassing associated with El Niño events is a long-lasting response that can persist about 1 year after the surface temperature anomaly has receded. This anomalous CO_2 drawdown stems from the ocean pCO_2 anomaly that originates in the near-equatorial Pacific band east of 160°E. In agreement with prior work, we find that the ocean pCO_2 anomaly close to the equator is controlled by changes in rainfall distribution that intensifies in the central and eastern equatorial Pacific, the eastward propagation of low-pCO_2 warm pool waters, as well as changes in vertical transport that modulate the relative contribution of subsurface waters to mixed-layer pCO_2 (e.g., Boutin et al., 1999; Feely et al., 2002; McKinley, Follows, et al., 2004). We find, however, that this near-equatorial pCO_2 anomaly is transported poleward by Ekman transport, yielding a doubling of the area and magnitude of the ocean CO_2 response (Figures 5 and 8). Prior work has examined the effect of Ekman transport in carrying salinity and heat anomalies (Alexander & Scott, 2008; Hasson et al., 2014, 2018; Vialard et al., 2001, 2002) but its significance for CO_2 fluxes had not been identified or quantified. The efficiency of this poleward amplification of the pCO_2 anomaly depends on both the wind-driven Ekman flow and the intensity and spatial distribution of the pCO_2 anomaly in the near-equatorial region. The southward Ekman flow efficiently exports the pCO_2

anomaly in the eastern Pacific, while the northward Ekman flow most efficiently exports the pCO_2 anomaly in the central Pacific.

Differences in the near-equatorial pCO_2 anomaly and its amplification by poleward Ekman transport control the evolution of the anomalous CO_2 drawdown. As could be expected, the CO_2 flux anomaly depends on the intensity of the El Niño event, with anomalous drawdowns up to 4 times stronger during strong (e.g., 2015/2016) and extreme (e.g., 1997/1998) events than during moderate events (e.g., 2002/2003). Yet the spatiotemporal evolution of the CO_2 flux is similar for moderate and strong central Pacific events, while extreme eastern Pacific El Niño events are characterized by a peculiar long-lasting CO_2 flux anomaly.

During central Pacific events, anomalous trade winds and rainfall recede in the boreal spring following the peak in El Niño 3.4 index (Ashok et al., 2007; Kao & Yu, 2009; Lengaigne & Vecchi, 2010; Vecchi, 2006; Vecchi & Harrison, 2006). As a result, the pCO_2 anomaly in the near-equatorial region, its poleward extension and the reduced CO_2 outgassing also subside in boreal spring. The near-equatorial pCO_2 anomalies in the central equatorial Pacific during these events lead to a strong amplification in the Northern Hemisphere in boreal winter (e.g., 2002/2003 and 2015/2016 events). The mixture of central and eastern Pacific dynamics during the 2015/2016 event (Paek et al., 2017) explains the broader eastward and southward extension of the CO_2 flux anomaly during this event compared to 2002/2003. Yet it is the dominant influence of the central Pacific dynamics that controls the intense amplification of the CO_2 flux anomaly northward and its decay in boreal spring.

The exceptional reduction in the CO_2 outgassing associated with the extreme eastern Pacific event of 1997/1998 was characterized by an unusual termination in boreal summer, that is, about 6 months later than during central Pacific events. In this event, the remarkably intense warming enabled the southward seasonal migration of the ITCZ in the far east equatorial Pacific, thereby inhibiting wind-driven upwelling and mixing in the equatorial band (Kao & Yu, 2009; Lengaigne & Vecchi, 2010; Vecchi & Harrison, 2006). We find that the sustained pCO_2 anomaly associated with this delayed termination yielded an intense reduction in CO_2 outgassing in the near-equatorial region and also its transport and amplification southward in boreal summer. The hemispheric asymmetry (northward extension in moderate and strong events vs. southward extension in extreme events) and the effect of seasonal phase locking on the termination of the anomalous CO_2 drawdown (i.e., boreal winter/spring for moderate and strong events vs. boreal summer for extreme events) found in the model are supported by the pCO_2-based product of Rödenbeck et al. (2013) (Figure 7).

Changes in freshwater fluxes have multiple effects on the ocean CO_2 response. The direct dilution effect on DIC and pCO_2 in the equatorial band was highlighted in previous studies (Christian et al., 2008; Doney et al., 2009; Turk et al., 2010). Our model suggests that this direct effect of rainfall accounts for about 15% of the pCO_2 drawdown in the near-equatorial region. However, we also find that rainfall can locally reinforce the effect of vertical dynamics and poleward transport through its effect on horizontal and vertical gradients of DIC, Alk, and salinity. Differences in the spatial distribution of rainfall between events therefore introduce disparities in the CO_2 response. For instance, in 2015/2016 and in 2002/2003, the northeastward migration of the south Pacific convergence zone (SPCZ) intensified the pCO_2 anomaly in the north central Pacific and enabled its northward amplification. In contrast, in 1997/1998, the southward migration of the ITCZ reinforced the pCO_2 anomaly in the equatorial band and its southward amplification by Ekman transport. We evaluated the overall effect of rainfall changes (direct effect of dilution + effect on vertical and horizontal gradients) using a crude model sensitivity experiment forced with climatological precipitations (but interannual wind, air temperature, humidity, etc.) between 2015 and 2016. In this experiment, the CO_2 flux response in the tropical Pacific Ocean (15°S to 15°N) is reduced by about 40% compared to the experiment with interannual changes in rainfall (not shown).

We find that the effect of thermal changes on the pCO_2 drawdown is very small compared to most other terms because of the compensation between the effect of air-sea heat flux and temperature transport by the ocean circulation (e.g., mixed-layer warming due to advection/mixing is rapidly compensated by air-sea heat loss to the atmosphere). Because heat is equilibrated much faster than pCO_2 at the air-sea interface (buffering effect of carbonates), changes in temperature associated with El Niño have a relatively small effect on oceanic pCO_2 and air-sea CO_2 fluxes. This might appear contradictory with prior work that identified thermal air-sea fluxes as a driver of CO_2 flux in the tropical Pacific Ocean (Lauderdale et al., 2016). The

framework proposed by Lauderdale et al. (2016) has however isolated the effect of air-sea heat flux from other thermal influences (transport by advection and mixing), while our framework considers the overall thermal effect.

A caveat of our approach is that the CO_2 flux response derived from the pCO_2 mixed-layer budget (i.e., change in pCO_2 equilibrated by the air-sea CO_2 flux) implicitly includes the effect of atmospheric variability (wind, pressure, and humidity, etc.) but it does not explicitly quantify their contribution to the spatial and temporal variability in the CO_2 response (Chiodi et al., 2019; McKinley, Follows, et al., 2004; Sutton et al., 2017). For instance, McKinley, Follows, et al. (2004) found that changes in wind speed explained 30% of the CO_2 flux interannual variability in the tropical Pacific Ocean. In addition, El Niño-driven changes in atmospheric pressure and humidity modulate the spatial distribution in atmospheric pCO_2 and amplify or dampen the local ocean CO_2 flux. For instance, we find that the anomalous CO_2 drawdown in the north central Pacific in 2016 was reinforced by a local decrease in atmospheric pCO_2. Another limitation of our model is the too shallow mixed-layer depth and associated high surface salinity bias in the central equatorial Pacific Ocean (Figures S1 and S6). This bias in the mean stratification might lead to the overestimation of the effect of vertical dynamics and freshwater dilution effect on pCO_2.

The pCO_2-based product of Rödenbeck et al. (2013) supports our findings on timing and meridional spatial variability between El Niño events. Yet the coverage of ocean pCO_2 observations in the tropical Pacific Ocean provides limited constraints on the spatial extent and temporal evolution of the ocean CO_2 response during El Niño events except at the equator where the TAO/TRITON array is located (Sutton, Feely, et al., 2014). The limited coverage most likely explains the strong discrepancies found in the spatiotemporal evolution of the CO_2 response between the two observation-based products (Landschützer et al., 2014; Rödenbeck et al., 2013) (Figures 2 and 7).

Satellite observations of atmospheric CO_2, such as the Orbital Carbon Observatory (OCO-2) mission which detected anomalies in column atmospheric CO_2 that were attributed to the ocean flux in the central Pacific (Chatterjee et al., 2017), could provide valuable complementary information to quantify the differences in magnitude and temporal evolution between El Niño events. We tested whether differences in the spatial and temporal evolution of the anomalous ocean CO_2 drawdown could be detected from space by comparing the atmospheric CO_2 anomaly expected from the ocean response during the El Niño events of 1997/1998 and 2015/2016 (Figure 9). The results suggest that differences in the magnitude and spatiotemporal pattern of the ocean CO_2 flux between the two events leave an imprint in atmospheric CO_2 gradients. The extreme eastern Pacific El Niño event of 1997/1998 yielded a basin-wide negative anomaly in atmospheric CO_2 up to −0.35 ppm that decayed at the end of boreal summer 1998, while the negative anomaly during the central Pacific event of 2015/2016 was weaker than −0.25 ppm and limited to the western Pacific Ocean. Analysis of the OCO-2 glint mode for version 7 data suggests that detection of this signature is feasible though challenging contingent on expected improvements in the retrieval algorithm (Kulawik et al., 2019; Worden et al., 2017). These improvements could augur a new era of observational constraints on oceanic fluxes and their partitioning described herein. Better understanding of the relative balance of these processes will provide more predictive skill as oceans respond to climate change.

Acknowledgments

Part of this research was carried out at the Jet Propulsion Laboratory, California Institute of Technology, under a contract with the National Aeronautics and Space Administration. We are very thankful to the NOAA-GFDL team that develops, maintains, and shares the ocean physical MOM6 code and the biogeochemical COBALT code, including A. Adcroft, J. Dunne, B. Hallberg, M. Harrison, and C. Stock. E. L., L. R., K. B., and J. L. gratefully acknowledge the support of the NASA OCO-2 Science Team Grant 80NSSC18K0893. K. B. and J. L. also acknowledge support from the NASA CMS-Flux NNH16ZDA001N-CMS.

Data Availability Statement

The MOM6 source code is publicly available at this site (https://github.com/NOAA-GFDL/MOM6-examples.git). The model data used in this study are publicly available on Zenodo (https://zenodo.org/record/3871069) under the https://doi.org/10.5281/zenodo.3871069.

References

Adcroft, A., Anderson, W., Balaji, V., Blanton, C., Bushuk, M., Dufour, C. O., et al. (2019). The GDDL global ocean and sea ice model OM4.0: Model description and simulation features. *Journal of Advances in Modeling Earth Systems*, *11*, 3167–3211. https://doi.org/10.1029/2019MS001726

Alexander, M. A., & Scott, J. D. (2008). The role of Ekman Ocean heat transport in the Northern Hemisphere response to ENSO. *Journal of Climate*, *21*(21), 5688–5707. https://doi.org/10.1175/2008JCLI2382.1

Ashok, K., Behera, S. K., Rao, S. A., Weng, H., & Yamagata, T. (2007). El Niño Modoki and its possible teleconnection. *Journal of Geophysical Research*, *112*, C11007. https://doi.org/10.1029/2006JC003798

Bacastow, R. B. (1976). Modulation of atmospheric carbon dioxide by the southern oscillation. *Nature*, *261*, 116–118. https://doi.org/10.1038/261116a0

Bakker, D. C. E., Pfeil, B., Landa, C. S., Metzl, N., O'Brien, K. M., Olsen, A., et al. (2016). A multi-decade record of high-quality fCO_2 data in version 3 of the Surface Ocean CO_2 Atlas (SOCAT). *Earth System Science Data*, *8*(2), 383–413. https://doi.org/10.5194/essd-8-383-2016

Banzon, V., Smith, T. M., Chin, T. M., Liu, C., & Hankins, W. (2016). A long-term record of blended satellite and in situ sea-surface temperature for climate monitoring, modeling and environmental studies. *Earth System Science Data*, *8*(1), 165–176. https://doi.org/10.5194/essd-8-165-2016

Behrenfeld, M. J., Randerson, J. T., McClain, C. R., Feldman, G. C., Los, S. O., Tucker, C. J., et al. (2001). Biospheric primary production during an ENSO transition. *Science*, *291*(5513), 2594–2597. https://doi.org/10.1126/science.1055071

Betts, R. A., Jones, C. D., Knight, J. R., Keeling, R. F., & Kennedy, J. J. (2016). El Niño and a record CO_2 rise. *Nature Climate Change*, *6*, 806–810. https://doi.org/10.1038/nclimate3063

Boutin, J., Etcheto, J., Dandonneau, Y., Bakker, D. C. E., Feely, R. A., Inoue, H. Y., et al. (1999). Satellite sea surface temperature: A powerful tool for interpreting in situ pCO_2 measurements in the equatorial Pacific Ocean. *Tellus B*, *51*(2), 490–508. https://doi.org/10.1034/j.1600-0889.1999.00025.x

Bowman, K. W., Liu, J., Bloom, A. A., Parazoo, N. C., Lee, M., Jiang, Z., et al. (2017). Global and Brazilian carbon response to El Niño Modoki 2011–2010. *Earth and Space Science*, *4*, 637–660. https://doi.org/10.1002/2016EA000204

Chatterjee, A., Gierach, M. M., Sutton, A. J., Feely, R. A., Crisp, D., Eldering, A., et al. (2017). Influence of El Niño on atmospheric CO_2 over the tropical Pacific Ocean: Findings from NASA's OCO-2 mission. *Science*, *358*, eaam5776. https://doi.org/10.1126/science.aam5776

Chavez, F. P., Strutton, P. G., Friederich, G. E., Feely, R. A., Feldman, G. C., Foley, D. G., & McPhaden, M. J. (1999). Biological and chemical response of the equatorial Pacific Ocean to the 1997–98 El Niño. *Science*, *286*(5447), 2126–2131. https://doi.org/10.1126/science.286.5447.2126

Chiodi, A. M., Dunne, J. P., & Harrison, D. E. (2019). Estimating air-sea carbon flux uncertainty over the tropical Pacific: Importance of winds and wind analysis uncertainty. *Global Biogeochemical Cycles*, *33*, 370–390. https://doi.org/10.1029/2018GB006047

Christian, J. R., Feely, R. A., Ishii, M., Murtugudde, R., & Wang, X. (2008). Testing an ocean carbon model with observed sea surface pCO_2 and dissolved inorganic carbon in the tropical Pacific Ocean. *Journal of Geophysical Research*, *113*, C07047. https://doi.org/10.1029/2007JC004428

Cox, P. M., Pearson, D., Booth, B. B., Friedlingstein, P., Huntingford, C., Jones, C. D., & Luke, C. M. (2013). Sensitivity of tropical carbon to climate change constrained by carbon dioxide variability. *Nature*, *494*(7437), 341–344. https://doi.org/10.1038/nature11882

Cronin, M. F., Gentemann, C. L., Edson, J., Ueki, I., Bourassa, M., Brown, S., et al. (2019). Air-sea fluxes with a focus on heat and momentum. *Frontiers in Marine Science*, *6*, 430. https://doi.org/10.3389/fmars.2019.00430

Dai, A., & Wigley, T. M. L. (2000). Global patterns of ENSO-induced precipitation. *Geophysical Research Letters*, *27*(9), 1283–1286. https://doi.org/10.1029/1999GL011140

de Boyer Montégut, C., Madec, G., Fischer, A. S., Lazar, A., & Iudicone, D. (2004). Mixed layer depth over the global ocean: An examination of profile data and a profile-based climatology. *Journal of Geophysical Research*, *109*, C12003. https://doi.org/10.1029/2004JC002378

Denvil-Sommer, A., Gehlen, M., Vrac, M., & Mejia, C. (2019). LSCE-FFNN-v1: A two-step neural network model for the reconstruction of surface ocean pCO_2 over the global ocean. *Geoscientific Model Development*, *12*(5), 2091–2105. https://doi.org/10.5194/gmd-12-2091-2019

Doney, S. C., Lima, I., Feely, R. A., Glover, D. M., Lindsay, K., Mahowald, N., et al. (2009). Mechanisms governing interannual variability in upper-ocean inorganic carbon system and air–sea CO_2 fluxes: Physical climate and atmospheric dust. *Deep Sea Research Part II: Topical Studies in Oceanography*, *56*(8–10), 640–655. https://doi.org/10.1016/j.dsr2.2008.12.006

Eddebbar, Y. A., Long, M. C., Resplandy, L., Rödenbeck, C., Rodgers, K. B., Manizza, M., & Keeling, R. F. (2017). Impacts of ENSO on air-sea oxygen exchange: Observations and mechanisms. *Global Biogeochemical Cycles*, *31*, 901–921. https://doi.org/10.1002/2017GB005630

Feely, R. A., Boutin, J., Cosca, C. E., Dandonneau, Y., Etcheto, J., Inoue, H. Y., et al. (2002). Seasonal and interannual variability of CO_2 in the equatorial Pacific. *Deep Sea Research Part II: Topical Studies in Oceanography*, *49*(13–14), 2443–2469. https://doi.org/10.1016/S0967-0645(02)00044-9

Feely, R. A., Wanninkhof, R., Takahashi, T., & Tans, P. (1999). Influence of El Niño on the equatorial Pacific contribution to atmospheric CO_2 accumulation. *Nature*, *398*(6728), 597–601. https://doi.org/10.1038/19273

Garcia, H. E., Boyer, T. P., Locarnini, R. A., Antonov, J. I., Mishonov, A. V., Baranova, O. K., et al. (2013). *World ocean atlas 2013. Volume 3, Dissolved oxygen, apparent oxygen utilization, and oxygen saturation*. In S. Levitus, & A. V. Mishonov (Eds.), (Technical Eds.), *NOAA Atlas NESDIS* (Vol. 75, p. 25). http://data.nodc.noaa.gov/woa/WOA13/DOC/woa13_vol3.pdf

Garcia, H. E., Locarnini, R. A., Boyer, T. P., Antonov, J. I., Baranova, O. K., Zweng, M. M., et al. (2013). *World ocean atlas 2013. Volume 4, Dissolved inorganic nutrients (phosphate, nitrate, silicate)*. In S. Levitus, & A. V. Mishonov (Eds.), (Technical Eds.), *NOAA Atlas NESDIS* (Vol. 76, p. 25). https://data.nodc.noaa.gov/woa/WOA13/DOC/woa13_vol4.pdf

Gelaro, R., McCarty, W., Suárez, M. J., Todling, R., Molod, A., Takacs, L., et al. (2017). The modern-era retrospective analysis for research and applications, version 2 (MERRA-2). *Journal of Climate*, *30*(14), 5419–5454. https://doi.org/10.1175/JCLI-D-16-0758.1

Gierach, M. M., Lee, T., Turk, D., & McPhaden, M. J. (2012). Biological response to the 1997–98 and 2009–10 El Niño events in the equatorial Pacific Ocean. *Geophysical Research Letters*, *39*, L10602. https://doi.org/10.1029/2012GL051103

Hasson, A., Delcroix, T., Boutin, J., Dussin, R., & Ballabrera-Poy, J. (2014). Analyzing the 2010–2011 La Niña signature in the tropical Pacific sea surface salinity using in situ data, SMOS observations, and a numerical simulation. *Journal of Geophysical Research: Oceans*, *119*, 3855–3867. https://doi.org/10.1002/2013JC009388

Hasson, A., Delcroix, T., & Dussin, R. (2013). An assessment of the mixed layer salinity budget in the tropical Pacific Ocean. Observations and modelling (1990–2009). *Ocean Dynamics*, *63*(2), 179–194. https://doi.org/10.1007/s10236-013-0596-2

Hasson, A., Puy, M., Boutin, J., Guilyardi, E., & Morrow, R. (2018). Northward pathway across the tropical North Pacific Ocean revealed by surface salinity: How do El Niño anomalies reach Hawaii? *Journal of Geophysical Research: Oceans*, *123*, 2697–2715. https://doi.org/10.1002/2017JC013423

Inoue, H. Y., Ishii, M., Matsueda, H., Saito, S., Aoyama, M., Tokieda, T., et al. (2001). Distributions and variations in the partial pressure of CO_2 in surface waters (pCO_2w) of the central and western equatorial Pacific during the 1997/1998 El Niño event. *Marine Chemistry*, *76*(1–2), 59–75. https://doi.org/10.1016/S0304-4203(01)00048-2

Ishii, M., Feely, R. A., Rodgers, K. B., Park, G. H., Wanninkhof, R., Sasano, D., et al. (2014). Air–sea CO_2 flux in the Pacific Ocean for the period 1990–2009. *Biogeosciences*, *11*(3), 709–734. https://doi.org/10.5194/bg-11-709-2014

Jones, C. D., Collins, M., Cox, P. M., & Spall, S. A. (2001). The carbon cycle response to ENSO: A coupled climate–carbon cycle model study. *Journal of Climate*, *14*(21), 4113–4129. https://doi.org/10.1175/1520-0442(2001)014<4113:TCCRTE>2.0.CO;2

Joos, F., & Spahni, R. (2008). Rates of change in natural and anthropogenic radiative forcing over the past 20,000 years. *Proceedings of the National Academy of Sciences*, *105*(5), 1425–1430. https://doi.org/10.1073/pnas.0707386105

Kao, H. Y., & Yu, J. Y. (2009). Contrasting eastern-Pacific and Central-Pacific types of ENSO. *Journal of Climate*, *22*(3), 615–632. https://doi.org/10.1175/2008JCLI2309.1

Keeling, C. D., & Revelle, R. (1985). Effects of El Niño/Southern Oscillation on the atmospheric content of carbon dioxide. *Meteoritics*, *20*, 437–450.

Keeling, C. D., Whorf, T. P., Wahlen, M., & Van der Plichtt, J. (1995). Interannual extremes in the rate of rise of atmospheric carbon dioxide since 1980. *Nature*, *375*(6533), 666–670. https://doi.org/10.1038/375666a0

Khatiwala, S., Tanhua, T., Mikaloff Fletcher, S., Gerber, M., Doney, S. C., Graven, H. D., et al. (2013). Global ocean storage of anthropogenic carbon. *Biogeosciences*, *10*(4), 2169–2191. https://doi.org/10.5194/bg-10-2169-2013

Kug, J. S., Jin, F. F., & An, S. I. (2009). Two types of El Niño events: Cold tongue El Niño and warm pool El Niño. *Journal of Climate*, *22*(6), 1499–1515. https://doi.org/10.1175/2008JCLI2624.1

Kulawik, S. S., O'Dell, C., Nelson, R. R., & Taylor, T. E. (2019). Validation of OCO-2 error analysis using simulated retrievals. *Atmospheric Measurement Techniques*, *12*(10), 5317–5334. https://doi.org/10.5194/amt-12-5317-2019

Kwiatkowski, L., Bopp, L., Aumont, O., Ciais, P., Cox, P. M., Laufkötter, C., et al. (2017). Emergent constraints on projections of declining primary production in the tropical oceans. *Nature Climate Change*, *7*(5), 355–358. https://doi.org/10.1038/nclimate3265

Landschützer, P., Gruber, N., Bakker, D. C. E., & Schuster, U. (2014). Recent variability of the global ocean carbon sink. *Global Biogeochemical Cycles*, *28*, 927–949. https://doi.org/10.1002/2014GB004853

Lauderdale, J. M., Dutkiewicz, S., Williams, R. G., & Follows, M. J. (2016). Quantifying the drivers of ocean-atmosphere CO_2 fluxes. *Global Biogeochemical Cycles*, *30*, 983–999. https://doi.org/10.1002/2016GB005400

Le Borgne, R., Feely, R. A., & Mackey, D. J. (2002). Carbon fluxes in the equatorial Pacific: A synthesis of the JGOFS programme. *Deep Sea Research Part II: Topical Studies in Oceanography*, *49*(13), 2425–2442. https://doi.org/10.1016/S0967-0645(02)00043-7

Le Quéré, C., Andrew, R. M., Friedlingstein, P., Sitch, S., Hauck, J., Pongratz, J., et al. (2018). Global carbon budget 2018. *Earth System Science Data*, *10*(4), 2141–2194. https://doi.org/10.5194/essd-10-2141-2018

Le Quéré, C., Orr, J. C., Monfray, P., Aumont, O., & Madec, G. (2000). Interannual variability of the oceanic sink of CO_2 from 1979 through 1997. *Global Biogeochemical Cycles*, *14*(4), 1247–1265. https://doi.org/10.1029/1999GB900049

Lengaigne, M., & Vecchi, G. A. (2010). Contrasting the termination of moderate and extreme El Niño events in coupled general circulation models. *Climate Dynamics*, *35*(2), 299–313. https://doi.org/10.1007/s00382-009-0562-3

Liu, J., Bowman, K. W., Lee, M., Henze, D. K., Bousserez, N., Brix, H., et al. (2014). Carbon monitoring system flux estimation and attribution: Impact of ACOS-GOSAT XCO_2 sampling on the inference of terrestrial biospheric sources and sinks. *Tellus B: Chemical and Physical Meteorology*, *66*, 22486. https://doi.org/10.3402/tellusb.v66.22486

Liu, J., Bowman, K. W., Schimel, D. S., Parazoo, N. C., Jiang, Z., Lee, M., et al. (2017). Contrasting carbon cycle responses of the tropical continents to the 2015–2016 El Niño. *Science*, *358*, eaam5690. https://doi.org/10.1126/science.aam5690

Locarnini, R. A., Mishonov, A. V., Antonov, J. I., Boyer, T. P., Garcia, H. E., Baranova, O. K., et al. (2013). *World ocean atlas 2013. Volume 1, temperature*. In S. Levitus, & A. V. Mishonov (Eds.), (Technical Eds.), *NOAA Atlas NESDIS* (Vol. 73, p. 40). https://data.nodc.noaa.gov/woa/WOA13/DOC/woa13_vol1.pdf

Lovenduski, N. S., Gruber, N., Doney, S. C., & Lima, I. D. (2007). Enhanced CO_2 outgassing in the Southern Ocean from a positive phase of the Southern Annular Mode. *Global Biogeochemical Cycles*, *21*, GB2026. https://doi.org/10.1029/2006GB002900

Maritorena, S., D'Andon, O. H. F., Mangin, A., & Siegel, D. A. (2010). Merged satellite ocean color data products using a bio-optical model: Characteristics, benefits and issues. *Remote Sensing of Environment*, *114*(8), 1791–1804. https://doi.org/10.1016/j.rse.2010.04.002

McKinley, G. A., Fay, A. R., Lovenduski, N. S., & Pilcher, D. J. (2017). Natural variability and anthropogenic trends in the ocean carbon sink. *Annual Review of Marine Science*, *9*(1), 125–150. https://doi.org/10.1146/annurev-marine-010816-060529

McKinley, G. A., Follows, M. J., & Marshall, J. (2004). Mechanisms of air-sea CO_2 flux variability in the equatorial Pacific and the North Atlantic. *Global Biogeochemical Cycles*, *18*, GB2011. https://doi.org/10.1029/2003GB002179

McKinley, G. A., Rödenbeck, C., Gloor, M., Houweling, S., & Heimann, M. (2004). Pacific dominance to global air-sea CO_2 flux variability: A novel atmospheric inversion agrees with ocean models. *Geophysical Research Letters*, *31*, L22308. https://doi.org/10.1029/2004GL021069

McPhaden, M. J., Busalacchi, A. J., Cheney, R., Donguy, J.-R., Gage, K. S., Halpern, D., et al. (1998). The tropical ocean-global atmosphere observing system: A decade of progress. *Journal of Geophysical Research*, *103*(C7), 14,169–14,240. https://doi.org/10.1029/97JC02906

McPhaden, M. J., Zebiak, S. E., & Glantz, M. H. (2006). ENSO as an integrating concept in earth science. *Science*, *314*(5806), 1740–1745. https://doi.org/10.1126/science.1132588

Meissner, T., Wentz, F. J., & Le Vine, D. M. (2018). The salinity retrieval algorithms for the NASA Aquarius version 5 and SMAP version 3 releases. *Remote Sensing*, *10*, 1121. https://doi.org/10.3390/rs10071121

Najjar, R., & Orr, J. (1998). Design of OCMIP-2 simulations of chlorofluorocarbons, the solubility pump and common biogeochemistry. Available at http://www.cgd.ucar.edu/oce/OCMIP/design.pdf

Nassar, R., Jones, D. B. A., Kulawik, S. S., Worden, J. R., Bowman, K. W., Andres, R. J., et al. (2011). Inverse modeling of CO_2 sources and sinks using satellite observations of CO_2 from TES and surface flask measurements. *Atmospheric Chemistry and Physics*, *11*(12), 6029–6047. https://doi.org/10.5194/acp-11-6029-2011

Nassar, R., Jones, D. B. A., Suntharalingam, P., Chen, J. M., Andres, R. J., Wecht, K. J., et al. (2010). Modeling global atmospheric CO_2 with improved emission inventories and CO_2 production from the oxidation of other carbon species. *Geoscientific Model Development*, *3*(2), 689–716. https://doi.org/10.5194/gmd-3-689-2010

Obata, A., & Kitamura, Y. (2003). Interannual variability of the sea-air exchange of CO_2 from 1961 to 1998 simulated with a global ocean circulation-biogeochemistry model. *Journal of Geophysical Research*, *108*(C11), 3337. https://doi.org/10.1029/2001JC001088

Olsen, A., Key, R. M., Heuven, S. V., Lauvset, S. K., Velo, A., Lin, X., et al. (2016). The Global Ocean Data Analysis Project version 2 (GLODAPv2) – An internally consistent data product for the world ocean. *Earth System Science Data*, *8*(2), 297–323. https://doi.org/10.5194/essd-8-297-2016

Paek, H., Yu, J. Y., & Qian, C. (2017). Why were the 2015/2016 and 1997/1998 extreme El Niños different? *Geophysical Research Letters*, *44*, 1848–1856. https://doi.org/10.1002/2016GL071515

Peylin, P., Law, R. M., Gurney, K. R., Chevallier, F., Jacobson, A. R., Maki, T., et al. (2013). Global atmospheric carbon budget: Results from an ensemble of atmospheric CO_2 inversions. *Biogeosciences*, *10*(10), 6699–6720. https://doi.org/10.5194/bg-10-6699-2013

Racault, M.-F., Sathyendranath, S., Brewin, R. J. W., Raitsos, D. E., Jackson, T., & Platt, T. (2017). Impact of El Niño variability on oceanic phytoplankton. *Frontiers in Marine Science*, *4*, 133. https://doi.org/10.3389/fmars.2017.00133

Rayner, N. A., Parker, D. E., Horton, E. B., Folland, C. K., Alexander, L. V., Rowell, D. P., et al. (2003). Global analyses of sea surface temperature, sea ice, and night marine air temperature since the late nineteenth century. *Journal of Geophysical Research*, *108*(D14), 4407. https://doi.org/10.1029/2002JD002670

Rödenbeck, C., Bakker, D. C. E., Gruber, N., Iida, Y., Jacobson, A. R., Jones, S., et al. (2015). Data-based estimates of the ocean carbon sink variability—First results of the Surface Ocean pCO_2 Mapping intercomparison (SOCOM). *Biogeosciences*, *12*(23), 7251–7278. https://doi.org/10.5194/bg-12-7251-2015

Rödenbeck, C., Bakker, D. C. E., Metzl, N., Olsen, A., Sabine, C., Cassar, N., et al. (2014). Interannual sea–air CO_2 flux variability from an observation-driven ocean mixed-layer scheme. *Biogeosciences*, *11*(17), 4599–4613. https://doi.org/10.5194/bg-11-4599-2014

Rödenbeck, C., Keeling, R. F., Bakker, D. C. E., Metzl, N., Olsen, A., Sabine, C., & Heimann, M. (2013). Global surface-ocean pCO_2 and sea–air CO_2 flux variability from an observation-driven ocean mixed-layer scheme. *Ocean Science*, *9*(2), 193–216. https://doi.org/10.5194/os-9-193-2013

Rödenbeck, C., Zaehle, S., Keeling, R., & Heimann, M. (2018). History of El Niño impacts on the global carbon cycle 1957–2017: A quantification from atmospheric CO_2 data. *Philosophical Transactions of the Royal Society of London. Series B, Biological Sciences*, *373*, 20170303. https://doi.org/10.1098/rstb.2017.0303

Roemmich, D., & Gilson, J. (2009). The 2004–2008 mean and annual cycle of temperature, salinity, and steric height in the global ocean from the Argo program. *Progress in Oceanography*, *82*(2), 81–100. https://doi.org/10.1016/j.pocean.2009.03.004

Sarmiento, J. L., & Gruber, N. (2006). *Ocean biogeochemical dynamics* (p. 318–355). Princeton, NJ: Princeton University Press.

Schneider, T., Bischoff, T., & Haug, G. H. (2014). Migrations and dynamics of the intertropical convergence zone. *Nature*, *513*(7516), 45–53. https://doi.org/10.1038/nature13636

Sellers, P. J., Schimel, D. S., Moore, B., Liu, J., & Eldering, A. (2018). Observing carbon cycle–climate feedbacks from space. *Proceedings of the National Academy of Sciences*, *115*(31), 7860–7868. https://doi.org/10.1073/pnas.1716613115

Stock, C. A., Dunne, J. P., & John, J. G. (2014a). Drivers of trophic amplification of ocean productivity trends in a changing climate. *Biogeosciences*, *11*(24), 7125–7135. https://doi.org/10.5194/bg-11-7125-2014

Stock, C. A., Dunne, J. P., & John, J. G. (2014b). Global-scale carbon and energy flows through the marine planktonic food web: An analysis with a coupled physical–biological model. *Progress in Oceanography*, *120*, 1–28. https://doi.org/10.1016/j.pocean.2013.07.001

Sutton, A. J., Feely, R. A., Sabine, C. L., McPhaden, M. J., Takahashi, T., Chavez, F. P., et al. (2014). Natural variability and anthropogenic change in equatorial Pacific surface ocean pCO_2 and pH. *Global Biogeochemical Cycles*, *28*, 131–145. https://doi.org/10.1002/2013GB004679

Sutton, A. J., Sabine, C. L., Maenner-Jones, S., Lawrence-Slavas, N., Meinig, C., Feely, R. A., et al. (2014). A high-frequency atmospheric and seawater pCO_2 data set from 14 open-ocean sites using a moored autonomous system. *Earth System Science Data*, *6*(2), 353–366. https://doi.org/10.5194/essd-6-353-2014

Sutton, A. J., Wanninkhof, R., Sabine, C. L., Feely, R. A., Cronin, M. F., & Weller, R. A. (2017). Variability and trends in surface seawater pCO_2 and CO_2 flux in the Pacific Ocean. *Geophysical Research Letters*, *44*, 5627–5636. https://doi.org/10.1002/2017GL073814

Taboada, F. G., Stock, C. A., Griffies, S. M., Dunne, J., John, J. G., Small, R. J., & Tsujino, H. (2019). Surface winds from atmospheric reanalysis lead to contrasting oceanic forcing and coastal upwelling patterns. *Ocean Modelling*, *133*, 79–111. https://doi.org/10.1016/j.ocemod.2018.11.003

Takahashi, T., Feely, R. A., Weiss, R. F., Wanninkhof, R. H., Chipman, D. W., Sutherland, S. C., & Takahashi, T. T. (1997). Global air-sea flux of CO_2: An estimate based on measurements of sea–air pCO_2 difference. *Proceedings of the National Academy of Sciences*, *94*(16), 8292–8299. https://doi.org/10.1073/pnas.94.16.8292

Takahashi, T., Olafsson, J., Goddard, J. G., Chipman, D. W., & Sutherland, S. C. (1993). Seasonal variation of CO_2 and nutrients in the high-latitude surface oceans: A comparative study. *Global Biogeochemical Cycles*, *7*(4), 843–878. https://doi.org/10.1029/93GB02263

Tsujino, H., Urakawa, S., Nakano, H., Small, R. J., Kim, W. M., Yeager, S. G., et al. (2018). JRA-55 based surface dataset for driving ocean–sea-ice models (JRA55-do). *Ocean Modelling*, *130*, 79–139. https://doi.org/10.1016/j.ocemod.2018.07.002

Turk, D., Meinen, C. S., Antoine, D., McPhaden, M. J., & Lewis, M. R. (2011). Implications of changing El Niño patterns for biological dynamics in the equatorial Pacific Ocean. *Geophysical Research Letters*, *38*, L23603. https://doi.org/10.1029/2011GL049674

Turk, D., Zappa, C. J., Meinen, C. S., Christian, J. R., Ho, D. T., Dickson, A. G., & McGillis, W. R. (2010). Rain impacts on CO_2 exchange in the western equatorial Pacific Ocean. *Geophysical Research Letters*, *37*, L23610. https://doi.org/10.1029/2010GL045520

Vecchi, G. A. (2006). The termination of the 1997–98 El Niño. Part II: Mechanisms of atmospheric change. *Journal of Climate*, *19*(12), 2647–2664. https://doi.org/10.1175/JCLI3780.1

Vecchi, G. A., & Harrison, D. E. (2006). The termination of the 1997–98 El Niño. Part I: Mechanisms of oceanic change. *Journal of Climate*, *19*(12), 2633–2646. https://doi.org/10.1175/JCLI3776.1

Vialard, J., Delecluse, P., & Menkes, C. (2002). A modeling study of salinity variability and its effects in the tropical Pacific Ocean during the 1993–1999 period. *Journal of Geophysical Research*, *107*(C12), 8005. https://doi.org/10.1029/2000JC000758

Vialard, J., Menkes, C., Boulanger, J.-P., Delecluse, P., Guilyardi, E., McPhaden, M. J., & Madec, G. (2001). A model study of oceanic mechanisms affecting equatorial Pacific Sea surface temperature during the 1997–98 El Niño. *Journal of Physical Oceanography*, *31*(7), 1649–1675. https://doi.org/10.1175/1520-0485(2001)031<1649:AMSOOM>2.0.CO;2

Wang, B., Luo, X., Yang, Y.-M., Sun, W., Cane, M. A., Cai, W., et al. (2019). Historical change of El Niño properties sheds light on future changes of extreme El Niño. *Proceedings of the National Academy of Sciences*, *116*(45), 22,512–22,517. https://doi.org/10.1073/pnas.1911130116

Wang, C., Deser, C., Yu, J.-Y., DiNezio, P., & Clement, A. (2012). El Niño and Southern Oscillation (ENSO): A review. In *Coral reefs of the eastern Pacific* (Vol. 8, p. 3–19). Dordrecht, Netherlands: Springer.

Wang, C., Deser, C., Yu, J.-Y., DiNezio, P., & Clement, A. (2017). El Niño and southern oscillation (ENSO): A review. In P. W. Glynn, D. P. Manzello, & I. C. Enochs (Eds.), *Coral reefs of the eastern tropical Pacific* (Vol. 8, p. 85–106). Dordrecht: Springer.

Wang, C., & Picaut, J. (2004). Understanding ENSO physics—A review. In C. Wang, S.-P. Xie, & J. A. Carton (Eds.), *Earth's climate: The ocean–atmosphere interaction*, *Geophysical Monograph Series* (Vol. 147, p. 21–48). Washington, DC: American Geophysical Union.

Wanninkhof, R. (1992). Relationship between wind speed and gas exchange over the ocean. *Journal of Geophysical Research*, *97*(C5), 7373–7382. https://doi.org/10.1029/92JC00188

Wanninkhof, R., Feely, R. A., Chen, H., Cosca, C., & Murphy, P. P. (1996). Surface water fCO_2 in the eastern equatorial Pacific during the 1992–1993 El Niño. *Journal of Geophysical Research*, *101*(C7), 16,333–16,343. https://doi.org/10.1029/96JC01348

Weiss, R. F., & Price, B. A. (1980). Nitrous oxide solubility in water and seawater. *Marine Chemistry*, *8*(4), 347–359. https://doi.org/10.1016/0304-4203(80)90024-9

Worden, J. R., Doran, G., Kulawik, S., Eldering, A., Crisp, D., Frankenberg, C., et al. (2017). Evaluation and attribution of OCO-2 XCO_2 uncertainties. *Atmospheric Measurement Techniques*, *10*(7), 2759–2771. https://doi.org/10.5194/amt-10-2759-2017

Yueh, S., Tang, W., Fore, A., Hayashi, A., Song, Y. T., & Lagerloef, G. (2014). Aquarius geophysical model function and combined active passive algorithm for ocean surface salinity and wind retrieval. *Journal of Geophysical Research: Oceans*, *119*, 5360–5379. https://doi.org/10.1002/2014JC009939

Zweng, M. M., Reagan, J. R., Antonov, J. I., Locarnini, R. A., Mishonov, A. V., Boyer, T. P., et al. (2013). *World Ocean Atlas 2013. Volume 2, Salinity*. In S. Levitus, & A. V. Mishonov (Eds.), *NOAA Atlas NESDIS* (Vol. 74, p. 39). https://data.nodc.noaa.gov/woa/WOA13/DOC/woa13_vol2.pdf